Systematic pseudopotentials from reference eigenvalue sets for DFT calculations

Pablo Rivero [a], Víctor Manuel García-Suárez [b], David Pereñiguez [a], Kainen Utt [a], Yurong Yang [a], Laurent Bellaiche [a], Kyungwha Park [c], Jaime Ferrer [b], Salvador Barraza-Lopez [a,*]

[a] Department of Physics, University of Arkansas, Fayetteville, AR 72701, USA
[b] Departamento de Física, Universidad de Oviedo and Centro de Investigación en Nanotecnología, Oviedo, Spain
[c] Physics Department, Virginia Polytechnic Institute and State University, Blacksburg, VA 24061, USA

A B S T R A C T

Pseudopotential-based Density-Functional Theory (DFT) permits the calculation of material properties with a modest computational effort, besides an acknowledged tradeoff of generating and testing pseudopotentials that reproduce established benchmark structural and electronic properties. To facilitate the needed benchmarking process, here we present a pragmatic method to optimize pseudopotentials for arbitrary materials directly from eigenvalue sets consistent with all-electron results. This method thus represents a much needed pragmatic route for the creation and assessment of sensitive pseudopotentials for DFT calculations that has been exemplified within the context of the *SIESTA* code. Comprehensive optimized pseudopotentials, basis sets, and lattice parameters are provided for *twenty chemical elements* in the bulk, and for both LDA and GGA exchange–correlation potentials. This method helps addressing the following issues: (i) the electronic dispersion and structural properties for Ge, Pd, Pt, Au, Ag, and Ta better agree with respect to all-electron results now, (ii) we provide the expected metallic behavior of Sn in the bulk – which comes out semiconducting when using available pseudopotentials, (iii) we create a validated pseudopotential for LDA-tungsten, and (iv) we create the first Bi pseudopotential for *SIESTA* that reproduces well-known electron and hole pockets at the *L* and *T* points. We investigated the transferability of these pseudopotentials and basis sets, and predict a new phase for two-dimensional tin as well.

1. Introduction

The search for new nanostructured materials is driven by Density Functional Theory (DFT) [1,2]. In the original approach to DFT all electrons are considered, but the electronic structure problem becomes simplified by the use of *pseudopotentials* (PPs) that capture the effect of the strong Coulomb potential from the nuclei and tightly bound (core) electrons as an effective ionic potential acting on the remaining (valence) electrons [3]. PPs are not unique: any PP leading to the proper phase shift (modulus 2π) is a valid one [4]. The basic requirement for a valid PP is the ability to reproduce all-electron results such as the electronic dispersion and structural parameters. The creation of accurate PPs is an ongoing endeavor, and two main *DFT* teams have updated their PP databases as recently as this year (*Abinit* [5] and *Quantum Espresso* [6]). The most recent *Abinit* PAW [7] database [5] does not include LDA datasets, and the older *Abinit* PAW dataset does not include Ge, Pd, Te, Ta, among other elements.

Here we extend this ongoing verification effort to Ref. [8] and corroborate that, out of twenty explored elements, the PPs available for C (atomic number 6), Al (13), Si (14), V (23), Cr (24), Cu (29), Se (34), Nb (41), and Te (52) – translations of the *Abinit* Fritz-Haber Institute Troullier–Martins [9] norm-conserving PPs (FHI-TM) [10]– perform well for both LDA [11,12] and GGA (PBE [13]) exchange–correlation potentials when compared to *VASP* results. This excellent performance occurs regardless of the specific basis set employed as long as the basis set is of DZP or larger size.

At the same time, the PPs for Ge (32), Pd (46), Ag (47), Sn (50), Sb (51), Ta (73), Pt (78), Au (79), and Bi (83) in Ref. [8] can be improved, and we demonstrate a viable route towards solving some of the following issues:

- *Ge (LDA and GGA):* While the *Abinit* FHI-TM pseudo opens a gap for Ge, all-electron band structures display a metallic behavior. It may be desirable to develop a Ge pseudo that reproduces all-electron results, if only for consistency across different DFT implementations.

- *Ag, Pd, Pt, Au, (LDA and GGA):* They have flatter lowermost bands than their all-electron counterparts and also display overestimated lattice constants a_0.
- *Sn (LDA and GGA):* It appears gapped, semiconducting, while it should be metallic.
- *W (LDA and GGA):* No PPs are available on the mentioned database [8] (a W PP is provided by Artacho and coworkers in Ref. [14]).
- *Bi and Sb (LDA and GGA):* Within the context of the *SIESTA* code [15–17] it is not easy to reproduce the electron and hole pockets [18] at the *L* and the *T* points induced by the spin–orbit interaction (SOI) [19].
- Magnetic elements Fe and Ni have been studied as well.

Faulty PPs for certain elements tend to occur for both LDA and GGA exchange–correlation potentials; this may be due to the usage of identical cutoff radii of the LDA and GGA PP input files for any given element. We also note that the PPs in Ref. [8] have no relativistic corrections which are necessary for heavier elements. For instance, the gap observed on bulk Sn closes down as soon as relativistic corrections are added to the PP inputs in Ref. [8].

The representation of a quantum mechanical state is not unique and any *complete* basis set can be used to expand electronic wavefunctions. According to Martin [3] there are three common choices for basis sets: plane waves, localized orbitals, and "augmented" functions. Plane-waves are the (systematic) basis set of choice in many DFT implementations (e.g., Refs. [18,22–24]). The *SIESTA* DFT code is based on localized basis sets known as Numerical Atomic Orbitals (NAOs) and it is formulated in a "tight-binding" language [3] which facilitates methodological developments for charge transport [25–28] and/or optical applications, or to include the effects of electron–electron correlations. The simulation speed goes down steeply in *SIESTA* as the number of NAOs is increased. On the other hand, for simulations containing only a few NAOs, the qualitative accuracy of the simulation depends on the choice of the PP and NAO parameters, and an acknowledged drawback of localized basis sets [15–17,29–35] is the lack of straightforward means for improving them to arbitrary precision [36].

Nevertheless, while numerical localized basis sets can be optimized following variational approaches [34], no method for the practical optimization of *SIESTA* PP input parameters exists and as seen in Fig. 1, upper subplot, *no additional work on the basis sets – e.g., larger size, variational optimization, and so on – will solve PP-related issues.*

Therefore, the objective of this Article is to lay out a *practical and reliable method* for the generation of norm-conserving PPs [37] to better reproduce all-electron bandstructures and structural properties within the context of the *SIESTA* code, thus representing a check and an update to Ref. [8].

The Article is structured as follows: We describe the problems being addressed in Section 2. Our algorithm is presented in Section 3. The results (Section 4) are divided in two parts: we tabulate twenty PPs, basis sets, and structural parameters in Tables 1–3, respectively, and provide a detailed discussion of these elements with largest discrepancies. Transferability is discussed in Section 5, and exemplified on a number of two-dimensional materials, the topological insulators Bi_2Se_3 and Bi_2Te_3 in the bulk and slabs, and magnetic dimers. We introduce the high-buckled phase of stanene in Section 6 to show how the results given here quickly produce novel Physics. We discuss execution times afterwards (Section 7), and provide concluding remarks in Section 8. For completeness, we share all those elements for which the PPs from Ref. [8] do produce results that agree reasonably well with *VASP* results as additional information.
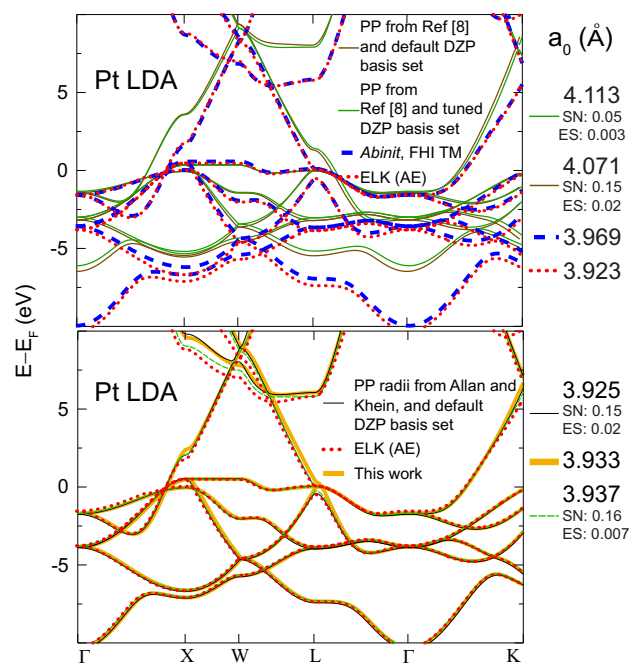

Fig. 1. Upper subplot: the Pt PP available on Ref. [8] fails to reproduce all-electron eigenvalues and a_0 from *ELK* [20] (red dotted), and those from *Abinit* with FHI-TM PPs (thick blue dashed line). This deficiency occurs regardless of DZP basis set employed (variationally tuned – SN and ES are the PAO.SplitNorm and PAO.EnergyShift (in Ry) parameters – or default: SN = 0.15 and ES = 0.02 Ry). Lower subplot (better PPs): using the radii from D.C. Allan and A. Khein [21] in the Pt PP one matches all-electron bands and shows the deficiency of the PP in Ref. [8]. We employed a default, non-tuned DZP basis set to obtain these results (thin black line). We propose here a pragmatic process to design PPs to match all-electron results (thick orange solid line) valid for elements for which PPs from Ref. [21] are not necessarily available. Further tuning of the NAO basis set does not diminish this improvement; see the overlapping dashed green line, using a variationally optimized DZP NAO basis set. (For interpretation of the references to colour in this figure legend, the reader is referred to the web version of this article.)

2. Statement of the problem

2.1. The PP on Ref. [8] does not seem to match the Abinit FHI-TM one [10]

As an example, Pt is an element for which one is unable to reproduce *ELK* [20] all-electron results with *SIESTA* using the PP in Ref. [8] regardless of basis set employed. We show in Fig. 1, upper subplot, results using a default DZP basis set with no tuning – brown thin solid line – and using a DZP basis set with PAO Energy Shift = 0.0031 Ry and PAO Split Norm = 0.052 that minimizes the total energy – green thin solid line. None of these results approach the all-electron bands displayed by the dotted red lines in Fig. 1. Further work on the basis set will not improve this situation.

We next perform an *Abinit* calculation using the Fritz-Haber-Institute Troullier Martins norm-conserving PP [10] shown by the blue dashed line in Fig. 1, upper subplot. The FHI-TM PP does lead to results consistent with all-electron calculations: the dotted *Abinit* and the dashed *ELK* band structures do overlap at almost every k-point (still, the *Abinit* lattice parameter, $a_0 = 3.969$ Å, overestimates the all-electron result (3.923 Å)).

SIESTA and *Abinit* calculations give different results using a PP which is nominally the same [8] (Fig. 1, upper subplot). We find this lack of agreement puzzling and problematic.

The lack of agreement among these *SIESTA* and *Abinit* results originates from the Pt PP in Ref. [8]. To demonstrate this assertion, we use the fdf input file employed in generating the *SIESTA* band structures for the upper subplot in Fig. 1 unchanged, but generate

Table 1
Inputs of Troullier–Martins norm-conserving PPs developed here for the *SIESTA* DFT code. To be compatible with the spin–orbit interaction, all PPs have relativistic corrections. Unless indicated otherwise, PPs are of the (pe) type: i.e., they include core corrections.

Element	Configuration	PP (rcut s, p, d, f; cfac, rcfac)
LDA		
C (6)	$2s^2 2p^2$	1.64(2s), 1.51(2p), 1.62(3d), 1.47(4f), –, – (pg)
Al (13)	$3s^2 2p^1$	2.30(3s), 2.19(3p), 2.06(3d), 2.17(4f), –, – (pg)
Si (14)	$3s^2 3p^2$	2.40(3s), 2.41(3p), 1.95(3d), 2.45(4f), –, – (pg)
V (23)	$4s^2 3d^3$	3.22(4s), 2.86(4p), 2.31(3d), 2.93(4f), 0.010, 0.000
Cr (24)	$4s^1 3d^5$	2.32(4s), 2.22(4p), 2.27(3d), 2.25(4f), –, – (pg)
Fe (26)	$4s^1 3d^7$	2.07(4s), 2.08(4p), 2.02(3d), 2.28(4f), 0.000, 0.684
Ni (28)	$4s^2 3d^8$	2.92(4s), 2.52(4p), 2.25(3d), 2.32(4f), 1.311, 0.000
Cu (29)	$4s^1 3d^{10}$	2.45(4s), 2.48(4p), 2.13(3d), 2.24(4f), –, – (pg)
Ge (32)	$3s^2 2p^1$	2.87(4s), 2.84(4p), 2.62(4d), 2.88(4f), –, – (pg)
Se (34)	$4s^2 4p^4$	3.23(4s), 2.40(4p), 2.46(4d), 2.16(4f), –, – (pg)
Nb (41)	$5s^1 4d^4$	2.93(5s), 2.91(5p), 2.59(4d), 2.12(4f), –, – (pg)
Pd (46)	$5s^1 4d^9$	2.01(5s), 2.45(5p), 2.01(4d), 2.25(4f), 0.016, 0.000
Ag (47)	$5s^1 4d^{10}$	2.70(5s), 2.71(5p), 2.22(4d), 2.58(4f), 0.007, 0.000
Sn (50)	$5s^2 5p^2$	3.30(5s), 3.42(5p), 3.36(5d), 2.84(4f), –, – (pg)
Te (52)	$5s^2 5p^4$	3.48(5s), 3.19(5p), 3.00(5d), 3.17(5f), 0.012, 0.000
Ta (73)	$6s^2 5d^3$	3.39(6s), 3.68(6p), 2.53(5d), 2.43(5f), –, – (pg)
W (74)	$6s^2 5d^4$	2.83(6s), 2.95(6p), 2.41(5d), 2.29(5f), 1.000, 0.000
Pt (78)	$5d^9 6s^1$	2.70(6s), 2.70(6p), 1.98(5d), 2.54(5f), 0.013, 0.000
Au (79)	$6s^1 5d^{10}$	2.63(6s), 2.77(6p), 3.06(5d), 2.80(5f), 0.009, 0.000
Bi (83)	$6s^2 6p^3$	3.10(6s), 2.00(6p), 3.55(6d), 2.75(5f), 0.000, 1.078
GGA		
C (6)	$2s^2 2p^2$	1.84(2s), 1.64(2p), 1.66(3d), 1.66(4f), –, – (pg)
Al (13)	$3s^2 2p^1$	3.08(3s), 2.20(3p), 2.38(3d), 2.69(4f), –, – (pg)
Si (14)	$3s^2 3p^2$	2.93(3s), 2.38(3p), 2.36(3d), 2.35(4f), –, – (pg)
V (23)	$4s^2 3d^3$	2.73(4s), 2.74(4p), 2.08(3d), 2.20(4f), 0.012, 0.000
Cr (24)	$4s^1 3d^5$	2.45(4s), 2.03(4p), 2.12(3d), 2.23(4f), 0.010, 0.000
Fe (26)	$4s^1 3d^7$	2.02(4s), 2.02(4p), 2.01(3d), 2.01(4f), 0.000, 0.645
Ni (28)	$4s^2 3d^8$	2.35(4s), 2.46(4p), 2.51(4d), 2.06(4f), 1.424, 0.000
Cu (29)	$4s^1 3d^{10}$	2.27(4s), 2.13(4p), 2.29(3d), 2.29(4f), –, – (pg)
Ge (32)	$4s^2 4p^2$	2.82(4s), 2.12(4p), 2.72(4d), 2.46(4f), –, – (pg)
Se (34)	$4s^2 4p^4$	2.11(4s), 3.80(4p), 2.16(4d), 2.59(4f), –, – (pg)
Nb (41)	$5s^1 4d^4$	2.72(5s), 2.48(5p), 2.68(4d), 2.56(4f), –, – (pg)
Pd (46)	$5s^1 4d^9$	2.48(5s), 2.48(5p), 2.16(4d), 2.48(4f), 0.014, 0.000
Ag (47)	$5s^1 4d^{10}$	2.19(5s), 2.83(5p), 2.40(4d), 2.82(4f), 0.010, 0.000
Sn (50)	$5s^2 5p^2$	2.59(5s), 2.15(5p), 3.75(5d), 2.69(4f), 0.008, 0.000
Te (52)	$5s^2 5p^4$	2.99(5s), 2.77(5p), 3.67(5d), 3.12(5f), 0.014, 0.000
Ta (73)	$6s^2 5d^3$	3.96(6s), 3.60(6p), 2.56(5d), 2.62(5f), –, – (pg)
W (74)	$6s^2 5d^4$	2.82(6s), 2.90(6p), 2.37(5d), 2.35(5f), 1.000, 0.000
Pt (78)	$6s^1 5d^9$	2.91(6s), 2.81(6p), 2.18(5d), 2.79(5f), 0.010, 0.000
Au (79)	$6s^1 5d^{10}$	2.50(6s), 3.42(6p), 2.98(5d), 3.42(5f), 0.012, 0.000
Bi (83)	$6s^2 6p^3$	3.10(6s), 2.00(6p), 3.55(6d), 2.75(5f), 0.000, 1.078

a new LDA Pt PP input file (INP) using the Allan–Khein cutoff radii [21] (no cutoff radii are directly available from FHI PP files) and replot the bandstructure without any special handling of the DZP basis set at the resulting equilibrium lattice constant $a_0 = 3.925$. Both bandstructures and a_0 match all-electron results now despite the DZP basis set being rather generic. The conclusion is that the Pt PP from Ref. [8] can be improved and, in this case, Allan–Khein [21] is shown to be a better alternative for Pt–LDA than Ref. [8] already.

As it will be shown on this Article, there are similar discrepancies on the electronic dispersion and the structural parameters for other elements, for which Allan–Khein PPs [21] are not necessarily available.

The process here described thus represents a viable answer to these problems.

We generate PPs *on the fly* by matching eigenvalues and lattice parameters versus *VASP* calculations with PAW PPs [38] which: (a) reproduce all-electron results reasonably well, albeit at a cheaper computational price, (b) are available for all chemical elements, for many exchange–correlation potentials, and for many valence electronic configurations. (Recall that *Abinit* has new PAW datasets only for GGA exchange–correlation [5], and that the previous *Abinit* PAW database lacks Ge, Pd, Te, and Ta PPs, which we successfully dealt with as well.) It is important to mention that Vanderbilt, Rabe

and coworkers contrasted some of their results against *VASP* during their recent PP deployment that was published on this Journal [6].

Pending the description of our algorithm, initial results are displayed for Pt in the bulk by the thick orange line in Fig. 1, lower subplot. The equilibrium lattice constant $a_0 = 3.933$ Å matches all-electron results better than *Abinit* with FHI-TM PPs [10] and those obtained with *SIESTA* using the PP input from Ref. [8]. To emphasize the improvement of the PP despite of the basis set employed, we show additional results with a variationally-tuned DZP basis set – PAO Energy Shift = 0.007 Ry and PAO Split Norm = 0.16, dashed green line – which, the reader will attest to, still remain closer to all-electron results than those displayed in Fig. 1, upper subplot.

2.2. The FHI-TM PP [10] misses some all-electron features

Consider Ge next: other known Troullier–Martins PPs do not close the electronic gap, thus failing to reproduce all-electron results. Indeed, all-electron band structures render Ge metallic and this behavior is reproduced by *VASP* too. This metallicity originates from the known underestimation of the electronic gap within DFT. We wish to realize consistent results for Ge across different DFT implementations.

Not consistent with all-electron results in Fig. 2, *Abinit* with PPs in Ref. [10] leads to a small gap for bulk Ge (LDA) and the PP from Ref. [8] has a similar shortcoming. Indeed, a larger ~1 eV electron gap occurs as long as the PP in Ref. [8] is employed despite the use of: (i) a default DZP basis set, (ii) a variationally tuned DZP basis set with SplitNorm and EnergyShift parameters written down in Fig. 2, and even (iii) a TZP basis set. This large gap is emphasized by the brown vertical line with arrows in Fig. 2.

We realize a Troullier–Martins, norm-conserving PP for Ge with a tendency towards closing this gap, in better agreement with all-electron results (see zoom-in in Fig. 2, right, where basis set analysis has been provided as well). Once a better PP has been determined – i.e., a PP with a significant tendency of closing the electronic gap – there is a basis set of DZP size that closes the gap entirely too (Tables 1 and 2).

A third example concerns the Ge PBE band structure. As seen in Fig. 3, left plot, the *SIESTA* dispersion with the PP in Ref. [8] and the *Abinit* dispersion with FHI-TM PPs (Ref. [10]) agree with all-electron results almost perfectly. But importantly, while the zoom-in indicates that *Abinit* resembles *ELK* all-electron data and yields a metallic Ge, *SIESTA* closes the gap gradually, and the shape of the bands around Γ is different from all-electron results. In contrast, the subplot on the right of Fig. 3 shows that the *SIESTA* PBE Ge dispersion with our PP input reproduces all-electron results and a_0 approaches its all-electron value too.

The results from Figs. 1–3 showcase the increased precision in *SIESTA* calculations with properly crafted PP inputs. We describe the process leading to those improved PPs next.

3. The algorithm: its origin, scope and limitations

It is good practice to benchmark *SIESTA* results with those obtained with other codes. We have benchmarked against *VASP* [39] in past work [40,41]. Back then, we found larger a_0's, and flatter bands for bulk Au when compared to *VASP* results.

The algorithm described here originated with the goal of finding NAO basis sets to better approach bandstructures obtained with a plane-wave code. Though the process is not variational, our starting assumption was that PPs from Ref. [8] are "good enough," such that the electronic dispersion from *SIESTA* and *VASP* could agree in principle. But the initial conclusion was that an optimization process that leaves PP inputs unchanged could never yield a genuine

Table 2
Optimized basis sets (a.u.). If so desired, readers can combine the PPs in Table 1 with other basis sets of their choice.

Element	Basis set	Y_i (eV)	Y_o (eV)	n_b	n_k
LDA					
C (6)	3.480, 2.761(2s), 3.758, 3.637(2p), 5.391(2d)	1061	1087	8	9^3
Al (13)	5.859, 4.513(3s), 6.809, 5.090(3p), 5.176(3d)	456	329	6	9^3
Si (14)	7.118, 6.130(3s), 6.517, 4.540(3p), 5.312(3d)	3248	3245	8	9^3
V (23)	6.804, 5.318(4s); 5.944, 4.203(3d); 4.435(4p)	3815	2868	8	9^3
Cr (24)	6.832, 6.332(4s), 5.551, 3.815(3d); 4.289(4p)	4471	3053	8	9^3
Fe (26)	8.100, 7.515, 6.632(4s); 6.001, 5.853(4p); 8.100, 5.037, 3.293 (3d)	69509	25519	10	21^3
Ni (28)	8.107, 6.006, 6.721(4s), 8.107, 5.042, 2.504(3d); 6.006, 5.713 (4p)	35298	34245	16	21^3
Cu (29)	6.622, 5.337(4s), 3.611, 2.469(3d), 4.643(3p)	1099	1004	8	9^3
Ge (32)	7.653, 5.861(4s), 7.494, 5.223(4p), 5.886(4d)	2875	2692	8	9^3
Se (34)	4.257, 3.619(4s), 5.331, 4.152(4p, polarized)	851	637	12	9^3
Nb (41)	6.619, 3.627(5s); 6.022, 4.292(4d); 5.711(5p)	3455	2413	8	9^3
Pd (46)	6.599, 6.097(5s), 4.735, 2.517(4d), 4.252(5p)	555	241	8	9^3
Ag (47)	6.520, 6.202(5s, polarized), 3.954, 2.553(4d)	1058	269	6	9^3
Sn (50)	5.275, 4.773(5s), 6.773, 5.615(5p, polarized)	2407	2615	8	9^3
Te (52)	5.106, 4.406(5s); 5.480, 4.507(5p); 5.464 (4d)	4043	3800	8	9^3
Ta (73)	6.008, 5.508(6s); 6.419, 4.260(5d); 4.008(6p)	2209	1772	8	9^3
W (74)	6.499, 5.181(6s); 6.311, 4.404(5d); 4.695(6p)	–	3002	8	9^3
Pt (78)	5.837, 5.048(6s), 5.319, 4.072(5d), 4.196(6p)	1952	383	8	9^3
Au (79)	6.083, 5.644(6s, polarized), 4.287, 2.838(5d)	2156	493	8	9^3
Bi (83)	6.153, 5.190, 4.584(6s); 5.456, 4.230(6p); 6.325, 5.103(6d)	26464	25607	4	15^3
GGA					
C (6)	4.067, 2.220(2s), 5.782, 3.641(2p), 3.395(2d)	992	1003	8	9^3
Al (13)	5.633, 2.542(3s), 4.762, 4.659(3p), 5.289(3d)	453	395	6	9^3
Si (14)	6.846, 4.925(3s), 6.676, 4.254(3p), 4.954(3d)	3202	3163	8	9^3
V (23)	4.632, 2.540(4s); 6.627, 3.927(3d); 4.824(4p)	3197	2438	8	9^3
Cr (24)	7.157, 5.157(4s); 5.555, 3.002(3d); 4.435(4p)	4402	3068	8	9^3
Fe (26)	8.100, 7.609, 6.715(4s); 6.001, 5.853(4p); 8.100, 5.037, 3.293(3d)	49770	24873	10	21^3
Ni (28)	8.107, 5.932, 6.721(4s), 8.107, 5.042, 2.504(3d); 6.006, 5.713(4p)	63151	59197	16	21^3
Cu (29)	5.501, 4.968(4s), 5.778, 3.996(3d), 4.431(4p)	931	776	8	9^3
Ge (32)	6.147, 5.009(4s), 7.392, 4.997(4p), 5.452(4d)	2688	2578	8	9^3
Se (34)	7.554, 4.189(4s); 5.810, 4.309(4p); 3.708(3d)	512	211	12	9^3
Nb (41)	6.299, 3.241(5s); 5.221, 3.133(4d); 4.861(5p)	3339	2716	8	9^3
Pd (46)	7.881, 3.823(5s), 7.555, 4.763(4d), 5.474(5p)	474	160	8	9^3
Ag (47)	5.777, 4.704(5s), 3.637, 3.137(4d), 6.514(5p)	1044	418	8	9^3
Sn (50)	7.275, 5.143(5s), 7.375, 4.490(5p), 4.170(5d)	2249	2121	8	9^3
Te (52)	4.836, 4.106(5s); 5.400, 4.697(5p); 5.877(4d)	1767	1481	8	9^3
Ta (73)	6.130, 3.094(6s); 6.594, 4.433(5d); 4.537(6p)	1782	1715	8	9^3
W (74)	4.052, 3.517(6s); 6.510, 4.342(5d); 5.459(6p)	3739	2832	8	9^3
Pt (78)	7.124, 5.621(6s), 4.161, 3.419(5d), 3.909(6p)	2086	249	8	9^3
Au (79)	6.083, 5.715(6s, polarized), 4.287, 2.838(5d)	2966	1027	8	9^3
Bi (83)	5.542, 5.348, 5.038(6s); 5.407, 4.562(6p); 6.601, 4.813(6d)	25967	24389	4	15^3

agreement for Au. This triggered the question whether the Au PP in Ref. [8] is "good enough".

To answer the question we took an unorthodox route by allowing the PP input parameters to vary within the optimization cycle. We found an immediate improvement of the dispersion and a_0 for bulk Au (the analysis for Au appears in Fig. 7): whenever a faulty (i.e., improvable) pseudo in Ref. [8] has been identified and a suitable replacement PP is locked-in by our algorithm, further work on the basis set does not change the closer agreement to all electron band structures and lattice parameters significantly. We demonstrate this by displaying additional band structures determined with variational DZP basis sets for the LDA plots in Figs. 1–5, 7, 8.

With the exception of Bi – the heaviest and most challenging element considered – we tuned LDA and GGA PPs separately. All PPs on this Article were generated with relativistic corrections so that they could be employed with the SOI implementation in SIESTA [19].

SIESTA eigenvalues E_s and structural parameters (a_0, c, positions of basis vectors) depend on PP and basis set inputs ($\xi_1,\ldots,\xi_m$) (i.e., $E_s = E_s(\xi_1,\ldots,\xi_m)$ and $a_0 = a_0(\xi_1,\ldots,\xi_m)$) which

can be tuned. Despite these parameters being tuned, the electron density is still subject to the standard DFT self-consistent cycle. As indicated before, one pragmatic way to tune said inputs may be to reduce the differences among eigenvalue sets on a dense k-point mesh and band i ($E_S(\xi_1,\ldots,\xi_m;i,k) - E_V(i,k) \to 0$) while ensuring that differences among structural parameters are small too. Successful PP inputs outperform those from Ref. [8] regardless of basis set used, and on systems different from those where tuning took place.

The starting point of the process is familiar to the novice user: We retrieve PP inputs from Ref. [8]; the basis set radii as specified from a SIESTA run in which default DZP basis sets were generated using said PP file; the starting DZP basis set takes default values for all parameters specifying size and shape.

We guide the SIESTA PPs towards a better agreement of the structural and electronic properties obtained with the VASP code [7,24,42–44] – which in all cases studied here showed a close resemblance to all electron results [20]. SIESTA uses numerical atomic orbital (NAO) basis sets with a strict radial cutoff [17,34] and core electrons are replaced by norm-conserving PPs [9]

Table 3
Lattice constants obtained with (i) *Abinit* and FHI-TM PPs [10], *SIESTA* with PPs from (ii) Ref. [8] and (iii) ours (Table 1), (iv) *VASP* with PAW PPs [38], *ELK* [20] using default inputs and a 21 × 21 × 21 *k*-point mesh, WIEN2K [56,57], and experiment [105]. Values of *c* have been reported as well. Di. stands for Diamond, and Rh. for rhombohedral structures, respectively. (Absolute percent discrepancies in parenthesis are indicated with respect to all-electron *ELK* values.)

	Structure	Abinit + Ref. [10]	SIESTA + Ref. [8] & default DZP basis	SIESTA + Tables 1 and 2	VASP	ELK	WIEN2K	Expt. [105]
LDA								
C (6)	Di.		3.542(0.03)	3.553(0.28)	3.534(0.25)	3.543	3.536	3.57
Al (13)	FCC		4.024(0.78)	3.959(0.85)	3.992(0.03)	3.993	3.983	4.05
Si (14)	Di.		5.410(0.15)	5.415(0.06)	5.402(0.30)	5.418	5.407	5.43
V (23)	BCC		2.887(1.80)	2.959(0.65)	2.910(1.02)	2.940	2.932	3.02
Cr (24)	BCC		2.779(0.68)	2.805(0.25)	2.778(0.71)	2.798		2.88
Fe (26)	BCC		2.889(4.86)	2.769(0.51)	2.749(0.22)	2.755	2.754	2.87
Ni (28)	FCC		3.529(2.86)	3.535(3.03)	3.421(0.29)	3.431	3.423	3.52
Cu (29)	FCC		3.609(2.12)	3.502(0.91)	3.523(0.31)	3.534	3.522	3.61
Ge (32)	Di.	5.573	5.616(1.32)	5.676(0.26)	5.646(0.79)	5.691	5.625	5.66
Se (34)	HCP		4.299,4.873	4.217,4.779	4.176, 5.142			4.37, 4.95
Nb (41)	BCC		3.216(1.02)	3.214(1.08)	3.263(0.43)	3.249	3.250	3.30
Pd (46)	FCC	3.942	3.922(1.69)	3.844(0.34)	3.840(0.44)	3.857	3.840	3.89
Ag (47)	FCC	4.213	4.091(3.52)	4.014(1.57)	4.015(1.59)	3.952	4.007	4.09
Sn (50)	Di.		6.457(0.12)	6.432(0.51)	6.475(0.15)	6.465	6.473	6.49
Te (52)	HCP		4.363, 5.795	4.326, 5.745	4.268, 5.967			4.46, 5.92
Ta (73)	BCC		3.245(1.25)	3.265(0.64)	3.245(1.25)	3.286		3.30
W (74)	BCC		3.152(0.32)	3.129(1.04)	3.162	3.143	3.17
Pt (78)	FCC	3.969	4.071(3.77)	3.933(0.25)	3.904(0.48)	3.923	3.909	3.92
Au (79)	FCC	4.187	4.268(6.22)	4.080(1.54)	4.064(1.14)	4.018	4.047	4.08
Bi (83)	Rh.		4.534	4.443	4.558			4.75
GGA								
C (6)	Di.		3.577(0.08)	3.584(0.28)	3.573(0.03)	3.574	3.575	3.57
Al (13)	FCC		4.077(0.37)	4.027(0.86)	4.047(0.37)	4.062	4.041	4.05
Si (14)	Di.		5.485(0.24)	5.466(0.11)	5.468(0.07)	5.472	5.475	5.43
V (23)	BCC		2.999(0.10)	3.018(0.53)	2.980(0.73)	3.002	3.001	3.02
Cr (24)	BCC		2.862(0.25)	2.897(1.47)	2.855(0.00)	2.855		2.88
Fe (26)	BCC		2.918(3.07)	2.862(1.10)	2.832(0.04)	2.831	2.833	2.87
Ni (28)	FCC		3.621(2.67)	3.582(1.56)	3.517(0.28)	3.527	3.518	3.52
Cu (29)	FCC		3.602(0.41)	3.669(1.44)	3.628(0.30)	3.617	3.632	3.61
Ge (32)	Di.	5.775	5.786(0.75)	5.818(0.21)	5.782(0.82)	5.830	5.763	5.66
Se (34)	HCP		4.380, 4.963	4.493, 5.092	4.426, 5.066			4.37, 4.95
Nb (41)	BCC		3.332(0.76)	3.294(0.39)	3.321(0.42)	3.307	3.312	3.30
Pd (46)	FCC	4.038	4.021(2.47)	3.985(1.55)	3.946(0.56)	3.924	3.942	3.89
Ag (47)	FCC	4.405	4.191(2.70)	4.089(0.20)	4.108(0.66)	4.081	4.152	4.09
Sn (50)	Di.		6.664(0.44)	6.672(0.56)	6.647(0.18)	6.635	6.655	6.49
Te (52)	HCP		4.486, 5.958	4.454, 5.915	4.508, 5.987			4.46, 5.92
Ta (73)	BCC		3.340(0.36)	3.369(0.51)	3.306(1.37)	3.352		3.30
W (74)	BCC		3.197(0.44)	3.195(0.50)	3.173(1.18)	3.211	3.191	3.17
Pt (78)	FCC	4.042	4.176(3.93)	3.969(1.22)	3.973(1.12)	4.018	3.985	3.92
Au (79)	FCC	4.323	4.370(4.10)	4.150(1.14)	4.174(0.57)	4.198	4.154	4.08
Bi (83)	Rh.		4.659	4.518	4.640			4.75

a_0 (Å): - - 5.573   — 5.616 SN: 0.15 ES: 0.02   — 5.627 SN: 0.21 ES: 0.005   —5.646   — 5.647 SN: 0.17 ES: 0.001   — 5.676   ⋯⋯ 5.691
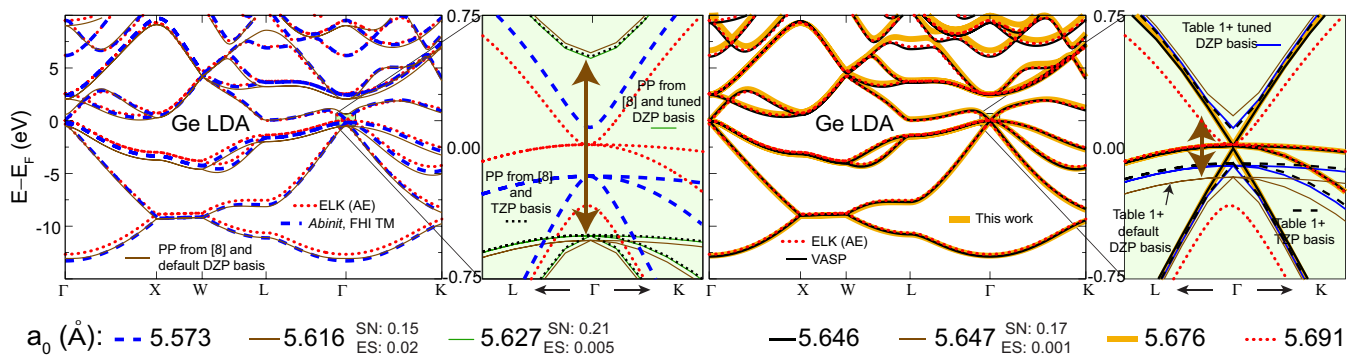
Fig. 2. The FHI parameterization of the Troullier–Martins norm-conserving PPs (FHI-NC-PPs) has shortcomings too: Ge is metallic within all-electron DFT, but *Abinit* band structures have electronic gaps when using FHI-NC-PPs (thick blue dashed line). A 1 eV gap shows up with *SIESTA* too [8]; no improvement of the basis set will help close this gap (DZP, TZP shown, gap is emphasized by a brown vertical line with arrows). Left: we create Troullier–Martins PPs for *SIESTA* that better reproduces all-electron band structures and lattice parameters a_0. (For interpretation of the references to colour in this figure legend, the reader is referred to the web version of this article.)

factorized in the Kleinman–Bylander form [45]. *SIESTA* PPs can include scalar-relativistic effects and nonlinear partial-core (pe) corrections [46]. Most NAO basis sets reported here are of *double-zeta plus polarization* (DZP) size [15]. *VASP* is based on partially-augmented wave (PAW) PPs [7,44] and a plane-wave

basis set [24,42,43]. Given different procedural approaches and approximations, one does not expect exact agreement among results obtained using these two codes. Nevertheless, the results obtained with the *ELK* code [20] after the optimization cycle help us corroborate the undeniable improvement in accuracy of the
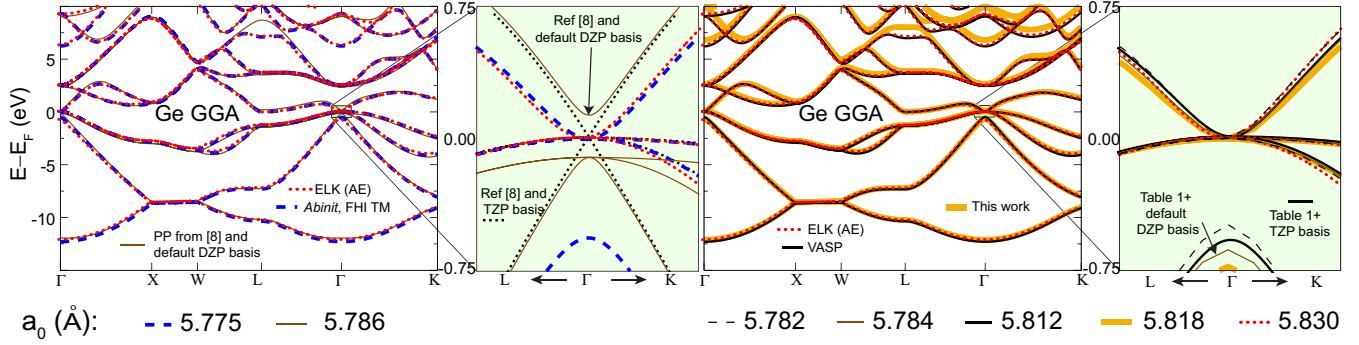
Fig. 3. Left: comparison of the *SIESTA* dispersion for Ge using GGA-PBE exchange correlation with the PP in Ref. [8] and a default DZP basis set (thin brown), the *Abinit* dispersion with FHI-TM PPs [10] (thick dashed blue), and the *ELK* all-electron code [20] (dotted red lines): the *SIESTA* dispersion with a default DZP basis shows a band gap, and the dispersion with a TZP basis – though closing the gap – does not reproduce all-electron behavior. Right: the PP for Ge PBE developed on this Article results on a correct band shape near the Fermi energy E_F regardless of the basis set employed (default DZP, tuned DZP, TZP), and consistent with all-electron DFT. (For interpretation of the references to colour in this figure legend, the reader is referred to the web version of this article.)
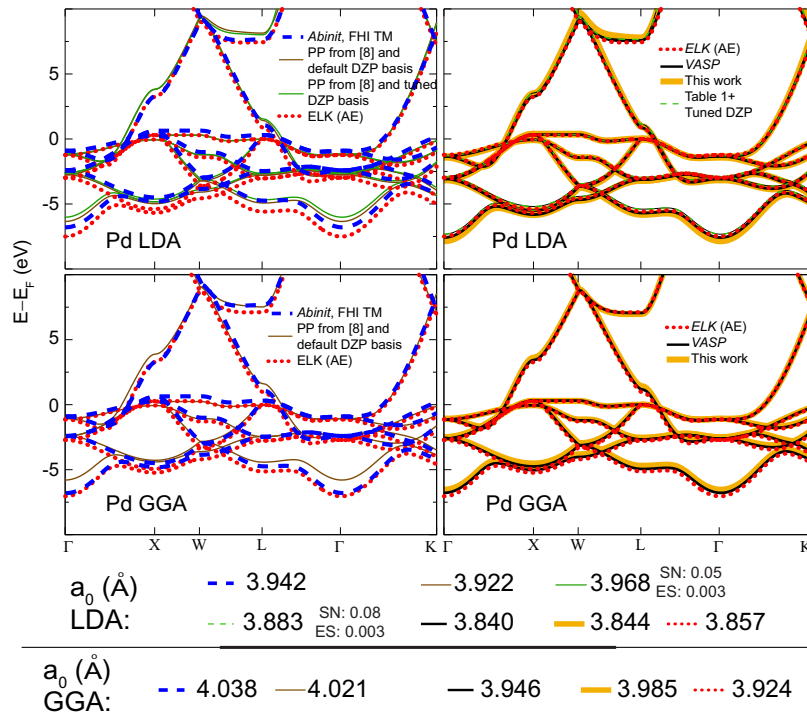
Fig. 4. Performance of the Pd PPs versus *ELK* all-electron results. *SIESTA* bandstructures (subplots obtained with the PP from Ref. [8] on the left subplot) do not match all-electron results in dotted red lines, regardless of basis set employed. On the other hand, the bandstructures on the plots to the right (thick orange, and dashed green) match visibly better both *VASP* and *ELK* band structures, regardless of basis set employed. Lattice constants a_0 are also shown here for a direct assessment of improvement of structural properties. (For interpretation of the references to colour in this figure legend, the reader is referred to the web version of this article.)

electronic dispersion and structural parameters arising from the optimization process.

This algorithm helps define and/or verify sensitive inputs for *SIESTA* calculations and, as featured in Figs. 1–3 already, it has the power to assist novice and seasoned users alike.

Consider a set of m initial parameters $(\xi_1^{(i)}, \ldots, \xi_m^{(i)})$ that encompasses PPs and NAO basis set inputs. The first four parameters are cutoff radii for the s, p, d, and f channels; i.e., they are the cutoff radii $r = r_c$ at which the logarithmic derivative of the all-electron radial wavefunction $R_l^{AE}(r,E)$ and the pseudo-wave function $R_l^{PP}(r,E)$ at energy E and angular momentum l agree for E close enough to the all electron eigenenergy E_l [9]:

$$\frac{1}{R_l^{PP}(r,E)} \frac{dR_l^{PP}(r,E)}{dr} = \frac{1}{R_l^{AE}(r,E)} \frac{dR_l^{AE}(r,E)}{dr}. \qquad (1)$$

For example, $\xi_1^{(i)}$ is the (cutoff) radius (r_c) for which Eq. (1) is satisfied for the $l = 0$ (s-channel), $\xi_2^{(i)}$ is the (cutoff) radius (r_c) for which Eq. (1) is satisfied for the $l = 1$ (p-channel), and so on. The first four parameters produce a harder PP the smaller a given cutoff becomes. Two additional parameters on the PP input are related to two distinct approaches to enforce core charge corrections.

The remaining parameters are cutoff radii r_c for the NAO basis set and they determine orbital localization/delocalization. A given NAO $\phi_{l,\xi}(r)$ has zero electronic density for $r > r_c$ [33]:

$$\phi_{l,\xi}(r) = 0. \qquad (2)$$

(We do not include soft-confining potentials nor other additional parameters in our NAO basis set [34].) For example, a basis of *standard* size requires five cutoff radii, so the parameter space would have a dimension $m = 5 + 5 = 10$. The points $(\xi_1, \ldots, \xi_m)$ on
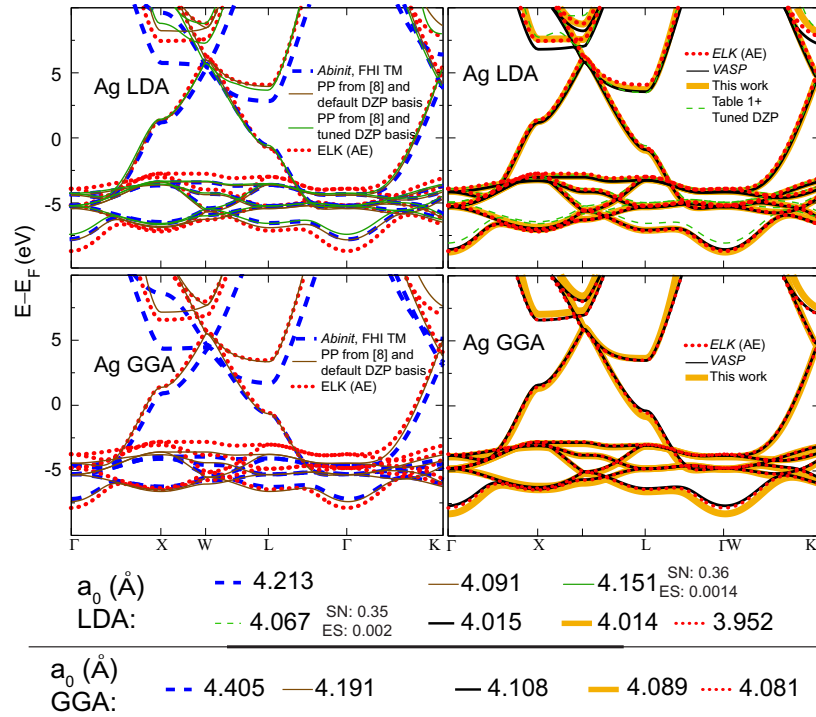
Fig. 5. Improving the performance of the Ag PPs: the rightmost subplots better approach all-electron results regardless of the specific basis set employed. Please refer to Fig. 4 for a description of each of the curves.

parameter space have physical bounds $\xi_j^{min} \leqslant \xi_j \leqslant \xi_j^{max}$ for $1 \leqslant j \leqslant m$. Specifically, we set the PP radii ($1 \leqslant j \leqslant 4$) to be in the $1.8 \leqslant \xi_j \leq 4.0$ Bohr range, and the basis radii ($6 < j \leqslant m$) within 1.5 and 8.0 Bohr, which were deemed sensible limits based on experience.

As extensively indicated, even though we vary both PP and basis set parameters simultaneously, *we lock a solid PP throughout the process*. The choice of the basis set is not important in comparison because, as expected, *in improving a faulty PP one reaches the most substantial agreement among SIESTA and all-electron eigenvalues and lattice parameters in spite of the particular basis set employed*.

Our process to create PPs and basis sets is intuitive:

1. With the starting choice of inputs to be optimized described previously, we first relax forces on bulk structures having a single chemical species.
2. Then, we use the *Simplex* algorithm [47] to guide the search for a parameter set $(\Xi_1, \ldots, \Xi_m)$ that best approximates *VASP* eigenvalues: the *Simplex* algorithm creates a sequential (systematic) search on parameter space $(\xi_1, \ldots, \xi_m)$ such that a function Y finds its smallest value; $Y(\Xi_1, \ldots, \Xi_m) \leqslant Y_i \equiv Y(\xi_1^{(i)}, \ldots, \xi_m^{(i)})$. Y is defined below.
3. The PPs and basis sets necessarily evolve during the parameter search. As a result, the equilibrium locations of atoms and the lattice constant a_0 must evolve as well: We obtain a new relaxed bulk structure once optimized inputs $Y(\Xi_1, \ldots, \Xi_m)$ are determined, and we report $Y_o = Y(\Xi_1, \ldots, \Xi_m)$ *on such relaxed structure*.

Y is a weighted cumulative absolute discrepancy between $E_V(i,k)$ and $E_S(\xi_1, \ldots, \xi_m; i, k)$ on n_b ($n_b = n_l + n_u$) bands around the Fermi level E_F and over a *dense mesh* that includes n_k k-points:

$$Y(\xi_1, \ldots, \xi_m) = \sum_{n=n_l}^{n_u} \sum_{k=1}^{n_k} w_{i,k} |E_V(i,k) - E_S(\xi_1, \ldots, \xi_m; i, k)|. \quad (3)$$
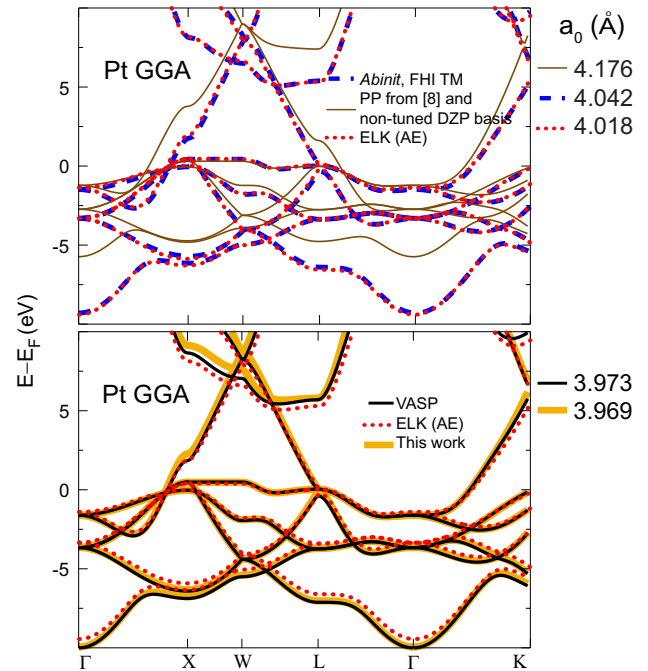

Fig. 6. Improving the performance of the Pt GGA PP: the lower subplots approach all-electron results consistently better. Please refer to Fig. 4 for a description of each of the curves.

Here E_V and E_s are *VASP* and *SIESTA* eigenvalues. The weight factor $w_{i,k} \geqslant 0$ in Eq. (3) becomes an additional control handle during the optimization cycle. For example, in order to lock-in electron and hole pockets for bulk Bi the weight factor was made comparatively large for the conduction and valence bands at the L and T k-points, where Bi electron/hole pockets are to be expected. Nevertheless, we reset $w_{i,k} \to 1$ for Y_i and Y_o when reporting those
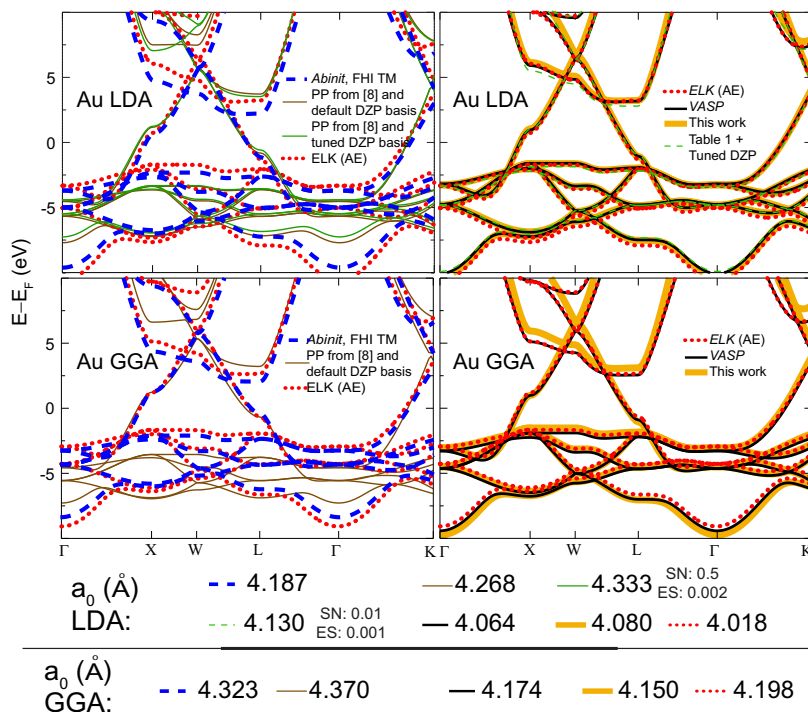
Fig. 7. Improving the performance of the Au PPs: the rightmost subplots approach all-electron results consistently better regardless of basis set employed. Please refer to Fig. 4 for a description of each of the curves.
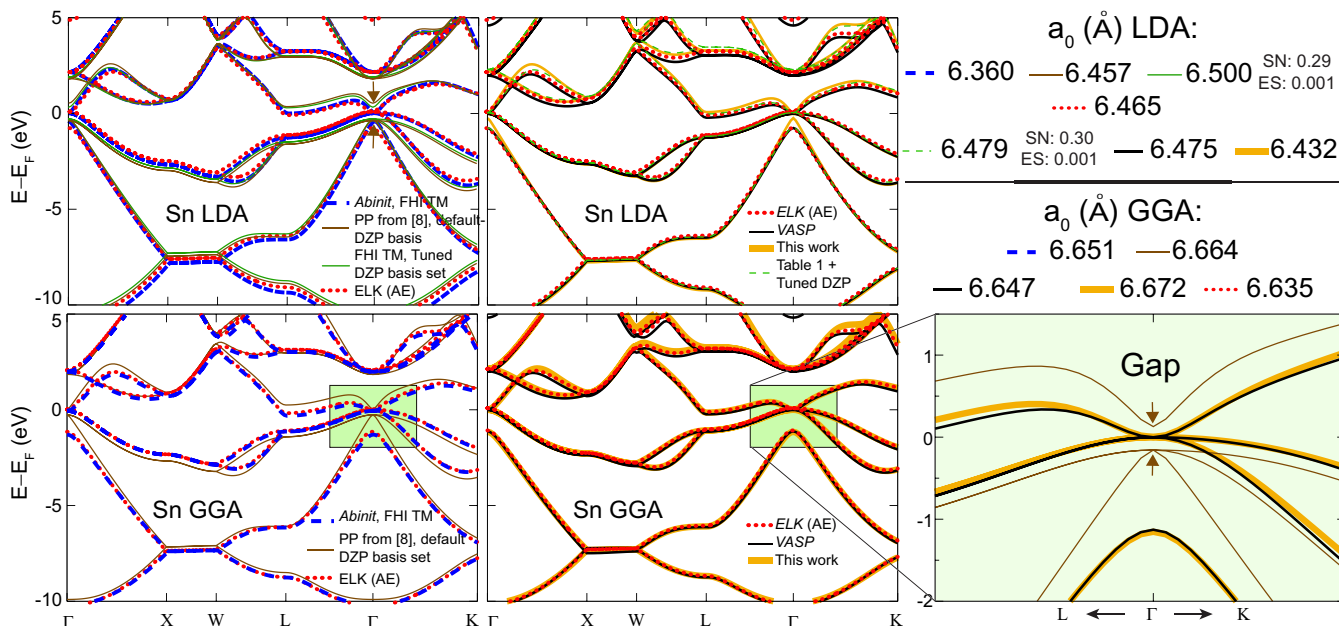

Fig. 8. Improving bulk Sn band structures. Our process leads to the correct dispersion and the expected metallic behavior for Sn.

values on this Article for a quantitative and systematic measure of the improvement on the electronic dispersion.

The algorithm works as follows: one runs *VASP* first to obtain an EIGENVAL file on the equilibrium structure. For consistency, the electronic configuration of the *VASP* PAW PP [38] will be identical to the configuration of the *SIESTA* PP to be optimized (Table 2). This means that the target for the *SIESTA* PP is to perform as well as the PAW one with the same valence configuration (systems requiring the promotion of core electrons into the valence – e.g., magnetic oxides – may require PP files different from the ones here provided).

We create an input INP file for the *ATM* program, and another input for the basis set which is stored on a basis.fdf file.

Upon execution, our algorithm first calls *ATM* to produce a *SIESTA* pseudopotential (psf file) from the INP file. With the psf file just created the algorithm calls *SIESTA* – which is executed in parallel mode – in order to generate an eigenvalue output file (EIG) on a dense k-point mesh using the psf and basis.fdf files. The algorithm records the absolute differences among the eigenvalues on the EIG file and those stored on a *VASP*'s EVALUES file, over n_b bands around E_F. (Care must be exercised that the k-point sets
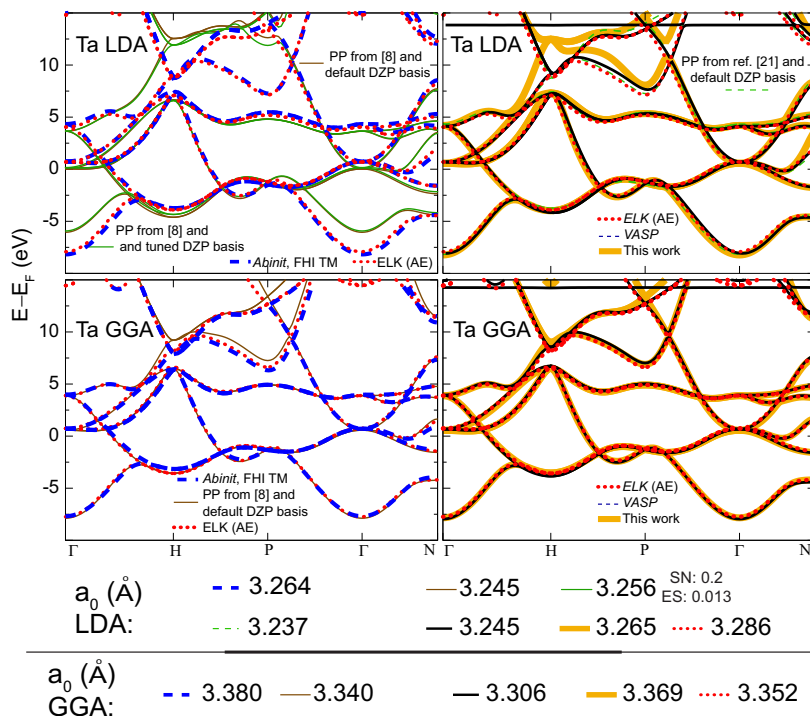
Fig. 9. Improving the performance of the Ta PPs: the rightmost subplots approach all-electron results consistently better regardless of basis set employed. Please refer to Fig. 4 for a description of each of the curves.
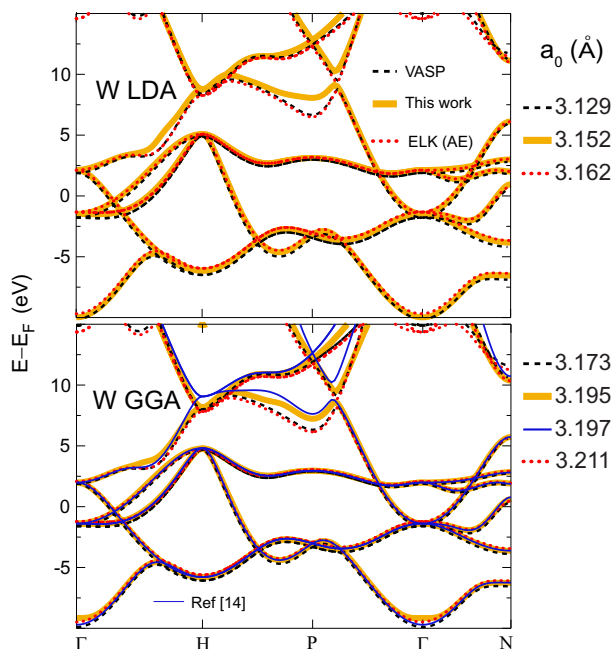
Fig. 10. Since there is no W PP on Ref. [8], the ability to propose and validate a W PP further highlights the usefulness of the present approach.

are consistent; this is accomplished by translating a *SIESTA* KP file onto a *VASP* KPOINTS file beforehand.)

Based upon the *Simplex* algorithm for the optimization in multidimensional spaces, the code establishes a new set of input parameters to continue to optimization cycle, and *ATM* and *SIESTA* continue to be called until the *Simplex* search reaches a point of no further improvement of the *SIESTA* eigenvalue sets.

The process described on this section streamlines the steps people follow in optimizing PPs and NAO basis sets. But it turns what

tends to be a human-based, visually-driven, and non-systematic parameter search onto a systematic, reliable, and quantitative numerical algorithm to quickly explore a remarkably vast number of input parameters.

3.1. Details of DFT calculations

A 400 eV energy cutoff was employed for *VASP* PAW [38] calculations. In *SIESTA* calculations, a 300 Ry cutoff was employed for the majority of the optimization runs; exceptions were Bi, Ni, and Fe, for which the cutoff was increased to at least 400 Ry.

Additional *Abinit* calculations with FHI-TM PPs [10] were performed on a $15 \times 15 \times 15$ k-point mesh, with a stringent cutoff energy of 40 Ry. All-electron calculations with the *ELK* code were done with standard input parameters and a $21 \times 21 \times 21$ k-point mesh. These additional calculations help identify substantial differences among results obtained with PPs in Refs. [8,10] and help monitoring the improvement in our results against an all-electron reference too.

4. Results

Optimized PP input parameters can be found in Table 1. Suggested basis sets can be found in Table 2. As usual within the *SIESTA* methodology, the reader is free to create other basis sets too. Values of Y_i and Y_o with PPs from Table 1 and basis sets from Table 2 are displayed in Table 2; the ratio Y_o/Y_i quantifies the optimization of the electronic dispersion. Structural information (lattice constants) are presented in Table 3 but we also display lattice constants on the figures for a quick visual assessment of improvement.

The eigenvalues and structural parameters will necessarily change with the use of a basis set different from the one in Table 2. Yet – as demonstrated on LDA plots – changes on a_0 and on the
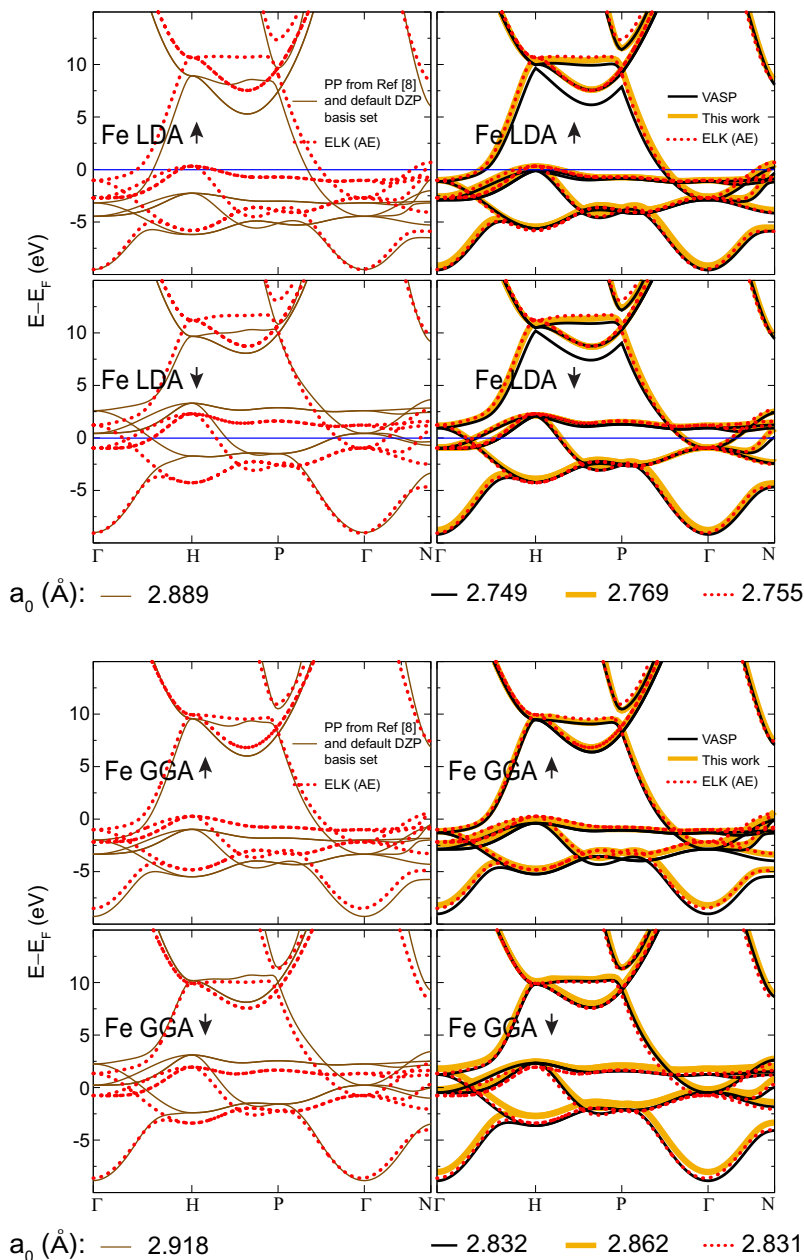
Fig. 11. Spin-resolved electronic dispersion for bulk BCC Fe.

electronic dispersion (hence Y_o) are small upon changes on a DZP basis set or a basis set of larger size.

We focus the discussion on Ge, Ag, Pd, Pt, Au, Sn, Ta, W, Fe, Ni, and Bi next.

4.1. Germanium

We have indicated that the dispersion for Ge agrees rather well in between *SIESTA* and *ELK*. As seen in Table 3, the lattice constants agree rather well too.

The important point here concerns the shape of the electron bands around E_F – zoom-in in Fig. 2. *VASP* displays a linear crossing not seen on the all-electron results. Given that we optimized the PP against *VASP*, the dispersion naturally reproduces *VASP* behavior. Despite this observation, the PP in Table 1 does close the ∼1 eV electronic gap and better reproduces all-electron results when compared to the dispersion obtained using the PP from Ref. [8].

4.2. Metals with bulk FCC crystal structure

Metal clusters and nanowires have been extensively studied with the *SIESTA* code (e.g., [48–52]). We now present results for FCC metals Ag, Pd, Pt, Au which are spin-unpolarized in the bulk.

One common feature on the band structures of these metals obtained with the PP from Ref. [8] concerns the lowermost band, which lies consistently higher in energy with respect to *VASP* (thick solid black lines) and *ELK* results (red dotted lines) in Figs. 1, 4–7. This discrepancy is particularly acute for Pt (Figs. 1 and 6), Pd LDA (Fig. 4), and Au (Fig. 7).

The agreement of the electronic dispersion and structural parameters towards *VASP* and *ELK* values when employing the PP inputs in Table 1 for Pt (Fig. 6), Pd GGA (Fig. 4), and Au (Fig. 7) must be pointed out. Band structures, obtained with the augmented-plane-waves method, can be found in Refs. [53–55] for Pd, Ag, Pt, Au, and Pd.

The PPs in Ref. [8] originate from Ref. [10], and *Abinit* calculations of bulk Pd, Ag, Pt, Au and Pd with PPs from [10] consistently overestimate all-electron values for a_0 (see Table 3 and Refs. [56,57]). The *Abinit* team has put effort on deploying newer PAW datasets [5] that supersede those from Ref. [10] and it makes sense for the *SIESTA* community to evaluate its PP inputs and to supersede those that perform poorly too.

The core corrections on many PPs from Ref. [8] and ours are tiny (e.g., V, Pd, Ag, Te, Pt, and Au), thus prompting questions whether eggbox effects may arise. (Not shown) calculations of the atomic separation of metallic dimers with the GGA-PBE exchange–correlation potential – for mesh cutoffs as small as 50 and 100 Ry – *display a single stable minima* thus discarding eggbox effects.

4.3. Metallic bulk tin

Tin (Sn) is a metal with a diamond structure and a strong spin–orbit coupling under normal conditions. Sn films can be grown on semiconductor substrates [58,59]. As it turns out, the *SIESTA* dispersion for bulk Sn does not capture the metallic behavior with the PP in Ref. [8] and a default DZP basis set. As we indicate in the opening lines of this Article, it is crucial to make sure the reference electronic dispersion in the bulk is reproduced before embarking on *SIESTA* calculations on other phases of Sn [60]. The gaps on bulk Sn serve to emphasize a point to always check inputs thoroughly.

4.4. Tantalum and tungsten

We discuss Ta next (Fig. 9). The lowermost band on the LDA plot has a too narrow bandwidth when compared to *Abinit*, *VASP*, and *ELK*; the upper-right subplot shows a solution.

We also provide optimized inputs for W taking as a starting PP radii the GGA parameters in Ref. [14] (see Fig. 10). Using a standard basis and the mentioned PP, a_0 becomes 3.152 Å. The possibility of creating reliable PPs – demonstrated for W-LDA here – increases
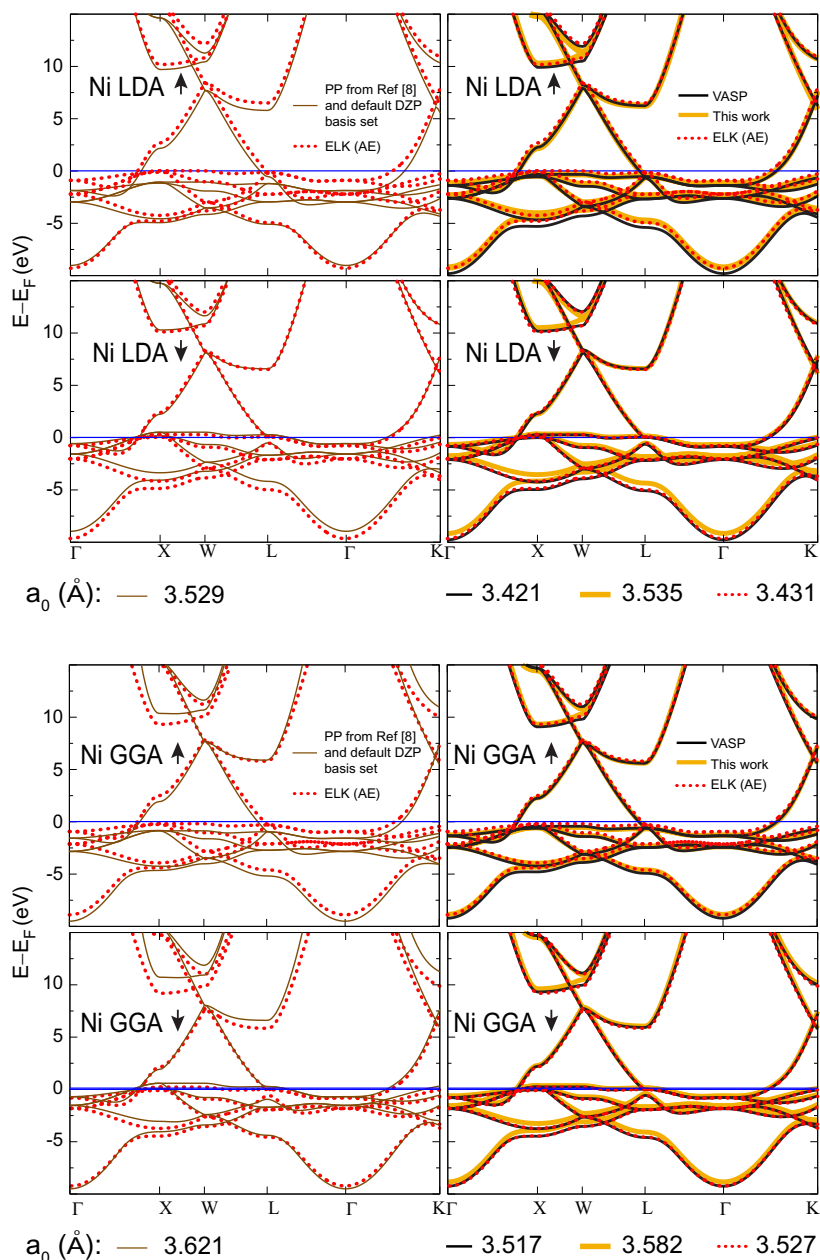

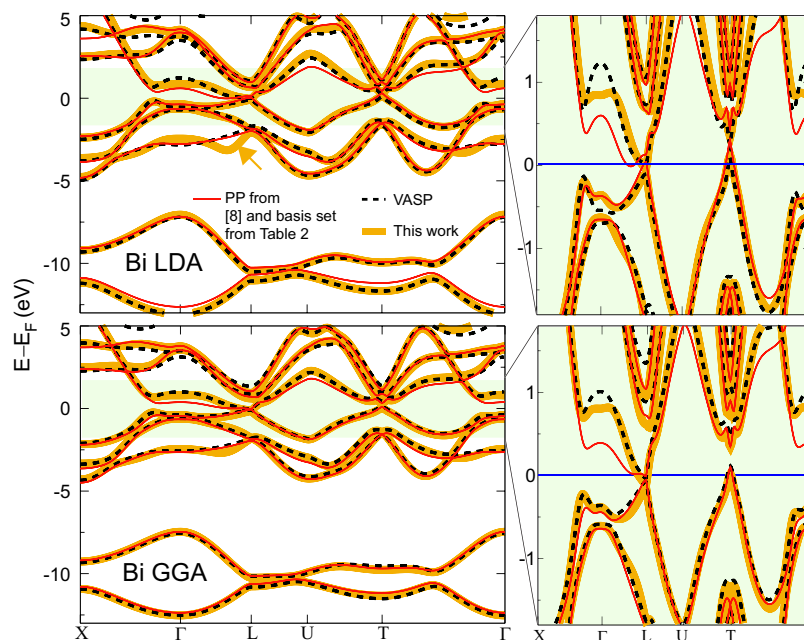Fig. 12. Spin-resolved electronic dispersion for bulk **FCC** Ni.

Fig. 13. Bulk Bi band structures displaying the pockets at *L*- and *T*-points when our PP is employed (see zoom-ins). The dashed black lines are *VASP* bands; red lines are obtained using the PP from [8] and the basis set from Table 2. Thick solid orange lines are bands with inputs from Tables 1 and 2. The single solid arrow in the LDA plot – a "kink" seen on the third band around the *L*-point – indicates that our PPs and basis sets differ with respect to both the *VASP* dispersion and to the dispersion in red there. Nevertheless, the improvement of the electronic dispersion remains substantial elsewhere, as seen by the overall band structures and the zoom-ins. (For interpretation of the references to colour in this figure legend, the reader is referred to the web version of this article.)

the value and usefulness of the present work. The LDA PP for W could be useful for studies of the transition metal dichalcogenide WSe$_2$ (See Fig. 15).

4.5. Iron and nickel

As it turns out, our PPs for Fe (Fig. 11) do not differ substantially from those in Ref. [61] after the optimization cycle, beyond some

differences on the *f*-channel for the LDA case, and on the core corrections determined from our optimization process for both LDA and GGA PPs (see Table 1 and Ref. [61]). The lattice parameter for Fe in Table 3 deviates from the *VASP* value by no more than 1% [38], and it is close to the *ELK* value too. We find magnetic moments $\mu = 2.01(1.99)$ Bohr magnetons (μ_B) for Fe LDA, and $\mu = 2.32(2.19)$ μ_B in our *SIESTA* (*VASP*) calculations (μ_B is the Bohr magneton). The reader must note the use of larger basis sets in
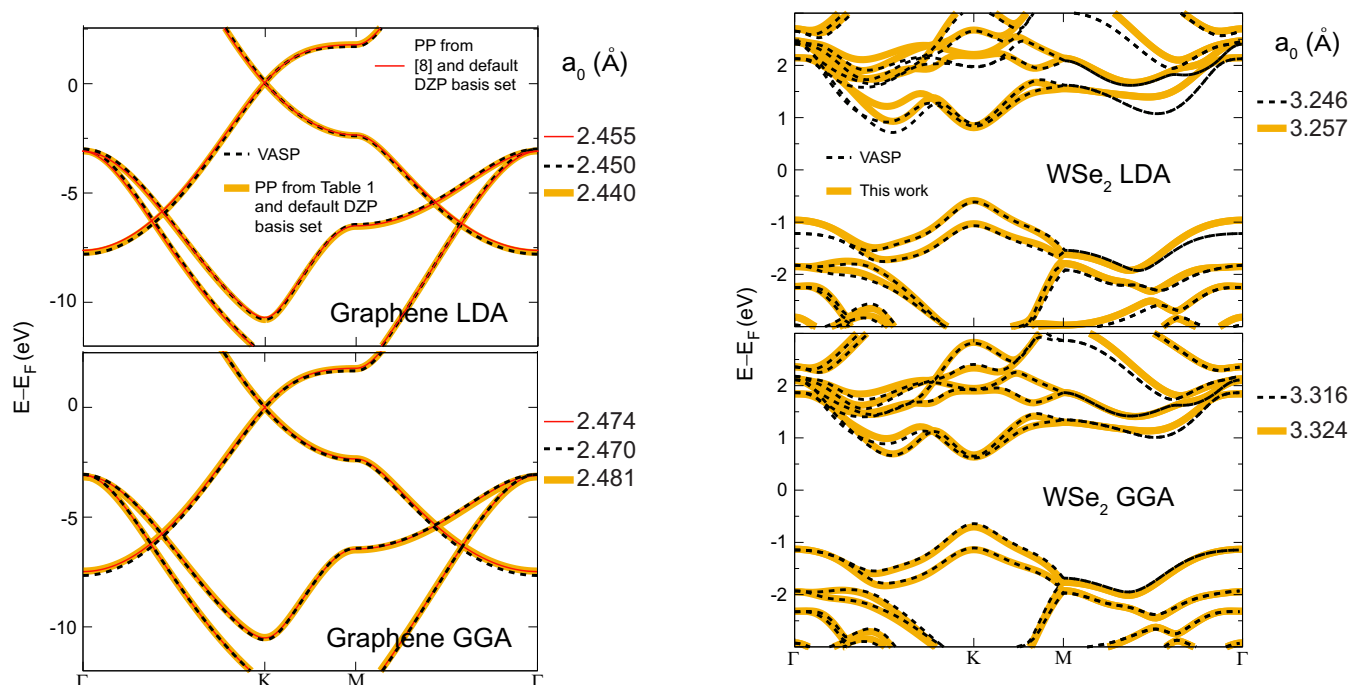

Fig. 14. Graphene. Note that the dispersion does not change significantly when our PP and other basis sets are used.

Fig. 15. Transition metal dichalcogenide WSe$_2$. The PP and basis sets employed on this work are from Tables 1 and 2. We verified that the dispersion does not change significantly with other basis sets.
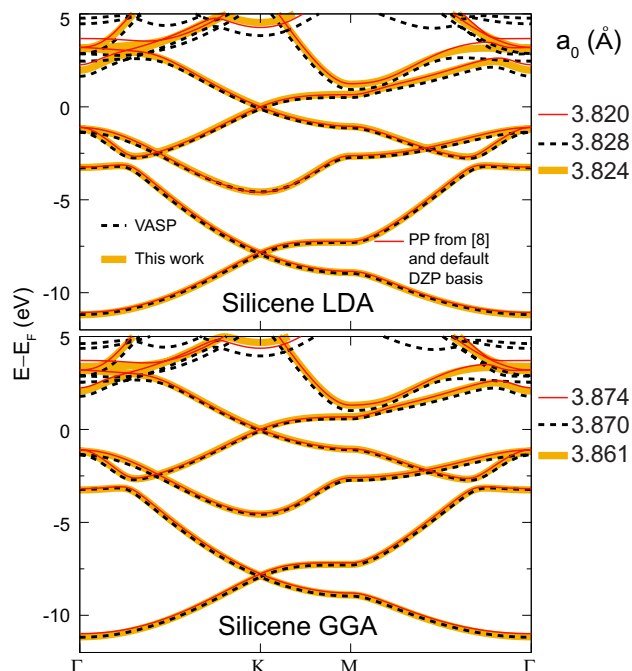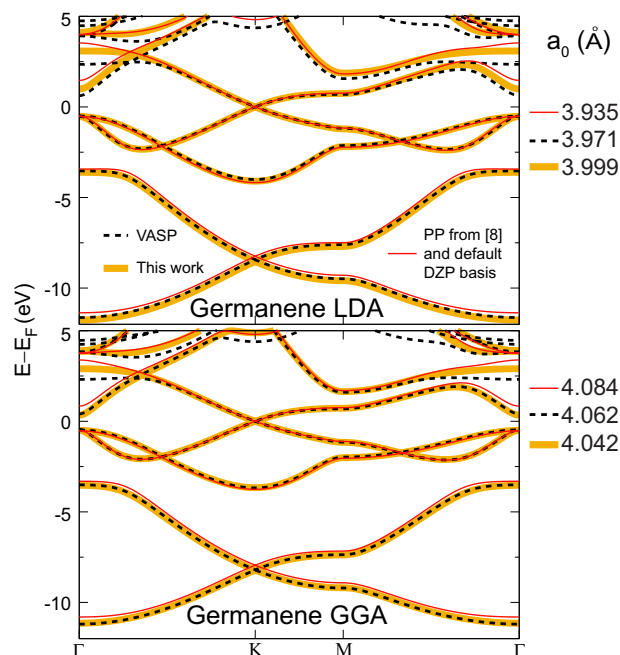
Fig. 16. Silicene. The PP and basis sets employed on this work are from Tables 1 and 2. We verified that the dispersion does not change significantly with other basis sets.

Fig. 17. Germanene. The PP and basis sets employed on this work are from Tables 1 and 2. We verified that the dispersion does not change significantly with other basis sets.

Table 2 for magnetic elements in order to increase the variational freedom.

The problem spotted for the up-channel of iron remains for nickel (Fig. 12): the two bands below E_F appear lower in energy than they ought to be, and this will lead to inaccurate magnetic moments as well. Using the PP from Table 1 and the basis from Table 2, the magnetic moments are 0.51/0.58 μ_B for LDA and 0.51/0.67 μ_B for PBE with VASP/SIESTA.

4.6. Bismuth

Bulk Bi is a group-V semimetal with a rhombohedral A7 structure at ambient conditions. The SOI leads to a *negative* indirect band gap of about 40 meV in between the high-symmetry *L*- and *T*-points, creating electron and hole pockets [62–66]. Though this process has been the most demanding of all, our algorithm guides us towards a Bi PP for SIESTA that reproduces these pockets. The structures are relaxed without explicit inclusion of the SOI, which was turned on to obtain the electronic dispersion. In order to bring to light the effect of the PP on the electronic dispersion we plot the Bi bandstructures in Fig. 13 using both Ref. [8] and ours (Table 1) with identical NAO basis sets on display in Table 2. This new Bi PP may be useful in quantum transport calculations for which a faithful description of the dispersion around E_F is important [67].

5. Transferability tests

We have demonstrated that the electronic and structural properties of specific structures can improve towards all-electron values by seeking agreement with VASP results.

Cautious readers would demand additional analysis and tests of these PPs on other systems. We report the transferability of these PPs on the following cases. (i) Two-dimensional materials made with these elements. (ii) Topological insulators Bi_2Se_3 and Bi_2Te_3. (iii) Metallic dimers.

5.1. Two-dimensional materials

SIESTA allows the characterization of two-dimensional systems at the DFT level with relatively large surface areas. The list of two-dimensional materials continues to grow with some well-established members (graphene [68–74], single-layer Boron Nitride [75], single layer transition metal dichalcogenides [76]), and some others materials being predicted or discovered just recently (e.g., Refs. [77–80]). An area of interest within 2D materials concerns the development of quantitative theory to couple the physical and chemical properties to non-planar geometries [81–86]: the premise is that the properties of 2D materials can be tuned by geometrical deformations.

5.1.1. Graphene
We next show the band structure of graphene [73,87] in Fig. 14.

5.1.2. Transition metal dichalcogenide WSe₂
There is a growing literature on transition metal dichalcogenides [88–94]. Transition metal dichalcogenides can acquire non-planar shapes such as polyhedra [95] and nanotubes [96,97]. In addition, being layered materials, they can be exfoliated to form single layer phases too (e.g., Ref. [98]). We compare the VASP and SIESTA band structures for single-layer WSe_2 in Fig. 15. As it has been found before, there is a direct gap at the *K*-point and the valence band becomes spin-polarized due to the SOI.

5.1.3. Silicene and germanene
We display a comparison of band structures for silicene and germanene [99] in Figs. 16 and 17.

5.2. Bi₂Se₃ and Bi₂Te₃ in the bulk and slabs

We next compare the electronic dispersion on an unrelaxed single-unit cell of bulk Bi_2Se_3. For this purpose we use the experimental lattice constant 9.841 Å and the rhombohedral angle $\alpha = 24.49°$, along with experimentally-derived atomic positions [100]. The electronic dispersion clearly matches the VASP results
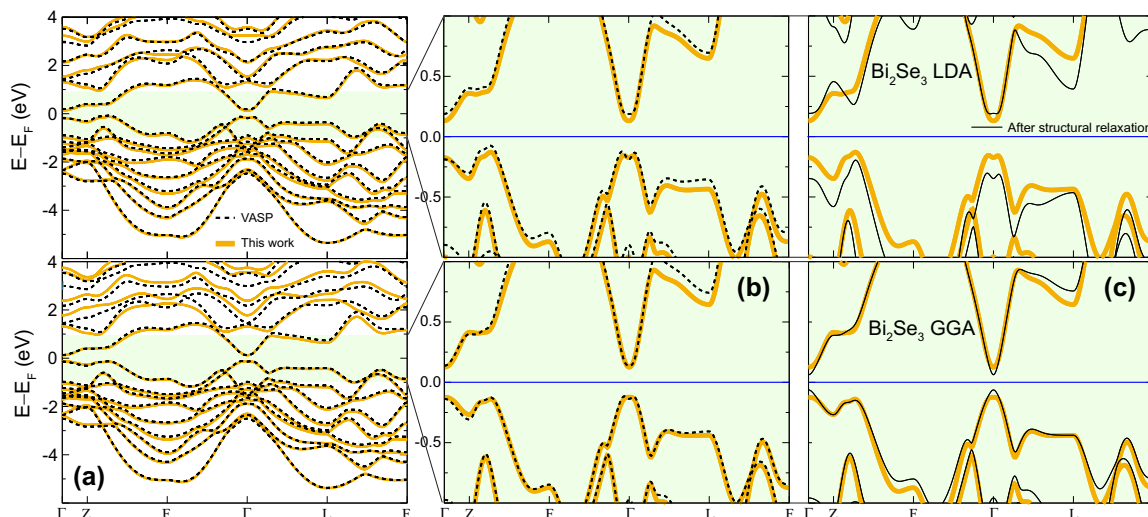
Fig. 18. Bulk Bi_2Se_3 band structures in the LDA and GGA approximations as a transferability test of the Bi and Se pseudopotentials and basis sets. Bandstructures reported in (a) and (b) were obtained on an identical (experimental) structure and no additional structural relaxation. We relax the bulk structure with SIESTA using optimized inputs; the electronic resulting dispersion can be seen in the thin black lines in subplot (c).
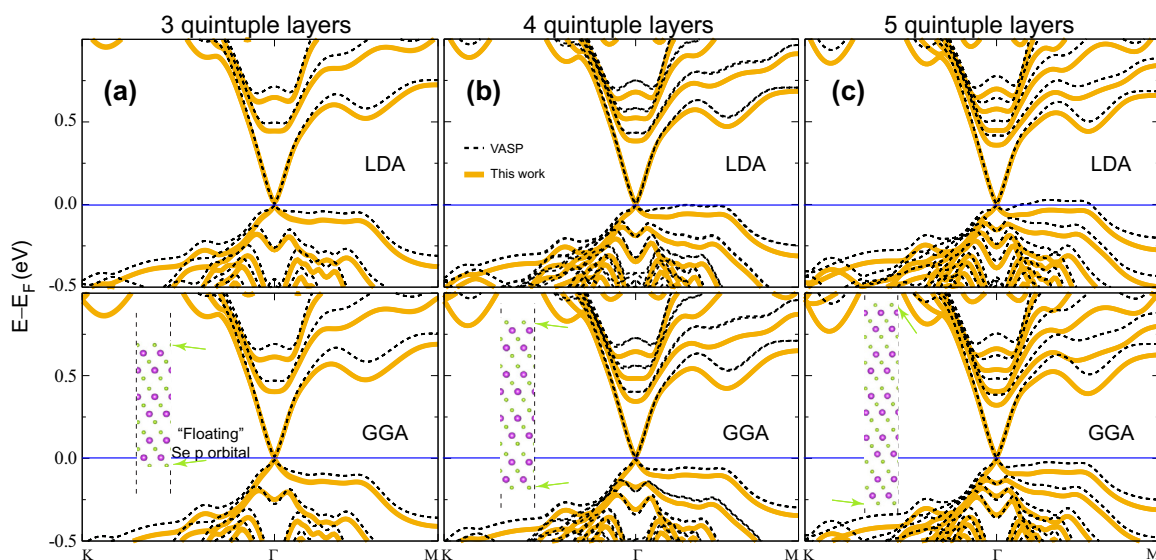

Fig. 19. Band structures for Bi_2Se_3 slabs with (a) three, (b) four, and (c) five quintuple layers.

for all bands below E_F (Fig. 18(a)). The agreement is arguably better around E_F too, as seen in Fig. 18(b).

Having validated our set of input parameters, we relax forces on these bulk structures, which is significantly more time-consuming using *VASP* (SOI off). The lattice parameter becomes $a_0 = 9.651$ Å (10.016 Å) after the structural relaxation for calculations with the LDA (GGA) XC potential ($\alpha = 24.49°$ remained unchanged). This presupposes a contraction with respect to experiment by 1.9% for the LDA structure, and a (symmetric) expansion of 1.8% for the structure obtained using the GGA exchange–correlation potential, which makes sense due to the known underestimation/overestimation of structural parameters in LDA/GGA. The thin black lines in Fig. 18(c) tell us that a lattice compression (LDA plot) opens the semiconducting gap further, while an isotropic elongation (GGA plot) closes it down with respect to its initial values (subplots Fig. 18(b) and (c)).

The calculation of the electronic dispersion for Bi_2Se_3 slabs is a more stringent transferability test. We display in Fig. 19 the electronic dispersion for slabs with three, four, and five quintuple layers relying on inputs from Tables 1 and 2. These slabs were built using the experimental lattice constant without additional structural relaxation. To increase the variational freedom of the *p*-surface states we added a "floating" *p*-orbital with a 6.5 Bohr radius to the two Se atoms facing the vacuum only, whose NAO basis description take this additional cutoff radius in addition to those indicated in Table 2. The addition of these two "floating" orbitals at the atoms facing the vacuum extend the variational freedom of surface states to improve the electronic dispersion [101] (more details on the effect of these "floating" *p*-orbitals will be given when we discuss Bi_2Te_3 slabs later on). The relative location of the Dirac point in Fig. 19 differs among *SIESTA* and *VASP*, with an apparent rigid vertical downshift of the *SIESTA* dispersion with inputs from Tables 1 and 2 with respect to the *VASP* dispersion (in dashed black lines). We turn to Bi_2Te_3 next.

The electronic dispersion for bulk Bi_2Te_3 in the experimental structure ($a_0 = 10.476$, $\alpha = 24.35°$ [102]) is displayed in Fig. 20. The dispersion does reflect *VASP* almost everywhere; the improvement around E_F is emphasized by zoom-ins in Fig. 20(b). We next
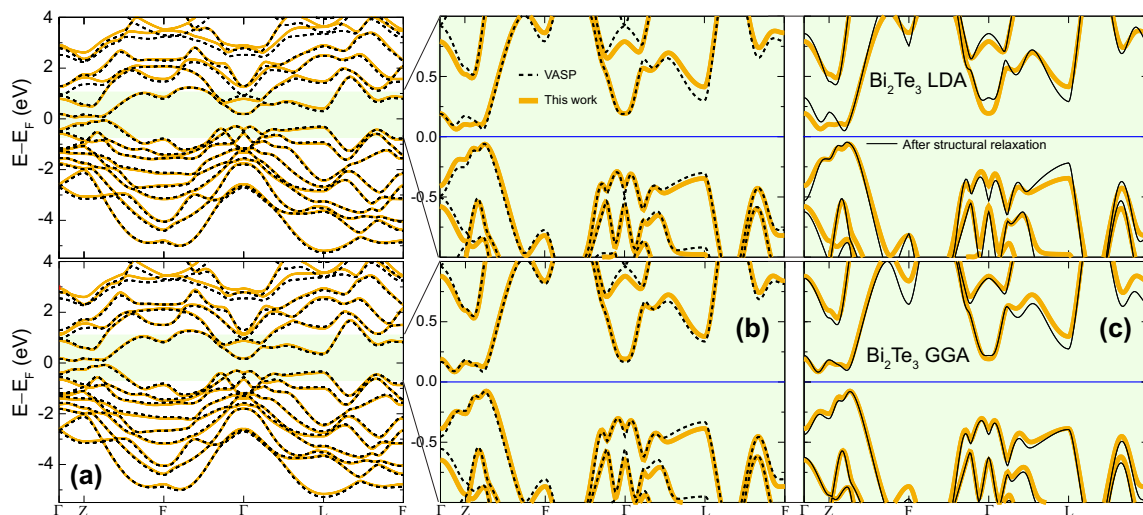
Fig. 20. Bulk Bi_2Te_3 band structures in the LDA and GGA approximations, as an additional transferability test. Band structures reported in (a) and (b) were computed using the experimental structure [102]. We relax the bulk with SIESTA using optimized inputs, and show the accompanying change in the electronic dispersion in (c). (d) Band structures for 3 quintuple-layer Bi_2Te_3 as a transferability test for the optimized PPs and basis sets. Here we make explicit the improvement of the electronic dispersion upon inclusion of the "floating" p-orbitals at two Te atoms facing the vacuum [101].
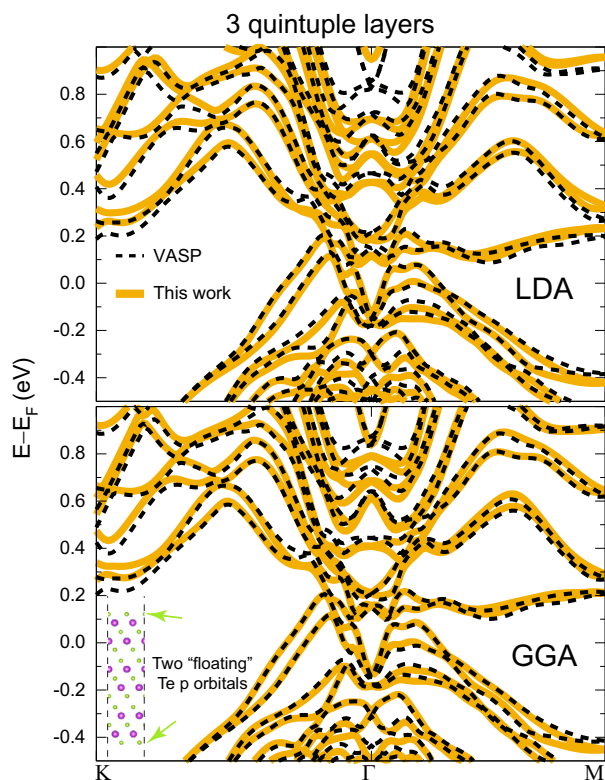

Fig. 21. Band structures for 3 quintuple-layer Bi_2Te_3 as a transferability test for the optimized pseudopotentials and basis sets.

relax the bulk atomistic structures and the cell parameters become $a_0 = 10.184$ Å, $\alpha = 24.53°$ ($a_0 = 10.664$ Å, $\alpha = 23.80°$) for calculations employing the LDA (GGA) exchange–correlation potential.

For Bi_2Te_3 slabs (Fig. 21) the crossing of linear bands occurs at energies within the bulk gap [103,104]. The dispersion obtained with *SIESTA* reproduces the *VASP* results; perhaps one discrepancy in Fig. 21 among bands from *VASP* and *SIESTA* with our optimized

Table 4
Magnetic moments and dimer lengths.

	VASP	*SIESTA* + Ref. [8]	*SIESTA* + Table 1
Pt_2	2.0 μ_B; 2.324 Å	2.23 μ_B; 2.400 Å	2.25 μ_B; 2.422 Å
Pd_2	2.0 μ_B; 2.484 Å	0.66 μ_B; 2.601 Å	1.83 μ_B; 2.460 Å
Au_2	0.14 μ_B; 2.525 Å	0.00 μ_B; 2.804 Å	0.00 μ_B; 2.604 Å
Fe_2	6.00 μ_B; 1.983 Å	6.00 μ_B; 2.426 Å	6.00 μ_B; 2.016 Å

inputs occurs around the Γ-point at the highest energies on that figure.

5.3. Dimers

A stringent test of transferability consists in taking the PPs from the bulk and contrasting lengths and magnetic moments in dimers. As reported in Table 4, our PPs agree with previously reported results [106,107]. All calculations were carried out using a TZP basis set, and with the GGA exchange–correlation functional. As indicated prior, dimer calculations were used to discard eggbox effects as well.

Put together, all the test on this section prove proper transferability of the PPs in Table 1.

6. Additional results

6.1. A new phase for stanene

Stanene is a single layer of tin with tunable electronic properties by chemical functionalization [60]. From a fundamental perspective, "low-buckled" (LB) stanene realizes a single-layer two-dimensional topological insulator with remarkable consequences from geometrical and topological considerations [108]. The electronic properties of "LB" stanene with LDA and GGA Sn PPs and the spin–orbit interaction turned on are shown in Fig. 22.

The phase recently introduced [60] resembles "low-buckled" (LB) silicene and germanene [99]. But unlike silicene and germanene, *stanene does have a stable "high-buckled" (HB) phase*, as seen by the phonon dispersion in Fig. 22 (lower-left plot). This new phase is metallic. See Ref. [109] for more details. We expect the *SIESTA* community to harness the validated PPs and basis sets on this
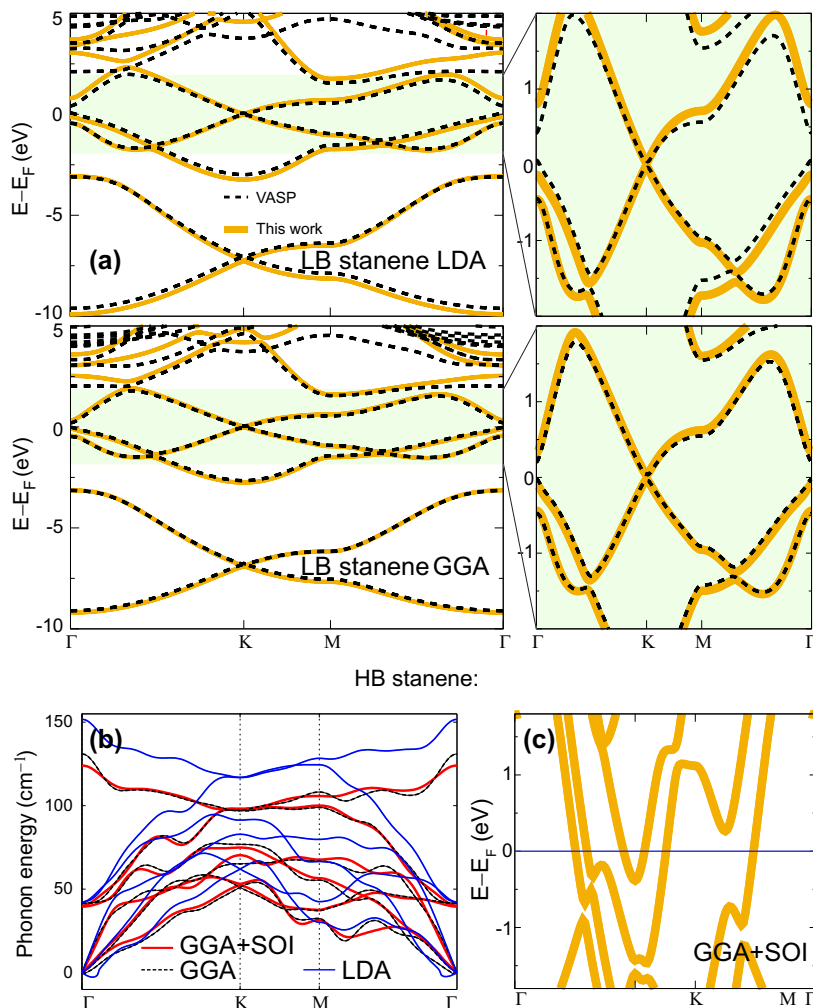
Fig. 22. (a) Comparison of stanene band structures. (b) We discovered that the HB phase is structurally stable given that the phonon dispersion curves show no significant negative energies. (c) The HB phase is metallic.

manuscript with the expectation that many other relevant results will be found.

7. Time and memory gains

The *SIESTA* Hamiltonian is sparse, which leads to drastic execution time savings in slab and molecular configurations given that the vacuum does not have to be filled with plane waves, as clearly illustrated in Table 5 for Bi_2Se_3. We employed a 350 Ry cutoff for

Table 5
Comparative execution times and memory usage for Bi_2Se_3 runs. Memory is given in Gb. Time is given in iterations per minute, and the number of cores employed are given in parenthesis. The word Qlayer stands for "quintuple layers."

System	k-Points	Precision	Mem.	Time
VASP				
Bulk	$9 \times 9 \times 9$	Medium	0.55	1.08 (16)
Bulk	$9 \times 9 \times 9$	Accurate	0.58	3.49 (16)
Bulk	$15 \times 15 \times 15$	Medium	1.93	4.76 (16)
3 Qlayers	$12 \times 12 \times 1$	Accurate	1.48	7.73 (48)
4 Qlayers	$12 \times 12 \times 1$	Accurate	1.74	11.70 (48)
SIESTA				
Bulk	$9 \times 9 \times 9$	–	1.51	0.36 (8)
Bulk	$15 \times 15 \times 15$	–	1.56	1.39 (16)
3 Qlayers	$12 \times 12 \times 1$	–	1.49	0.85 (16)
4 Qlayers	$12 \times 12 \times 1$	–	1.67	1.32 (16)

SIESTA calculations, and precision flags Medium and High on the *VASP* code. *SIESTA* runs proceed sequentially on *k*-points, as reflected on the almost identical memory usage regardless of the number of *k*-points employed. The slabs had a 16 Å vacuum along the vertical direction.

Regardless of calculation reported, we observe in Table 5 speed-ups ranging from 3× (Bulk, $9 \times 9 \times 9$, Medium precision) to 20× (Bulk, $9 \times 9 \times 9$, high precision) per core.

8. Conclusions

So far there is no known procedure to optimize *SIESTA* PPs in the literature. As a result, the optimization procedures (when they are carried out) become extremely time-consuming and prone to deliver a non-optimized set of inputs that may lead to errors. This is a *de facto* barrier for a more widely use of the *SIESTA* methodology. This Article represents a comprehensive and validated database of PPs for *SIESTA* DFT calculations. A thorough analysis has been provided to highlight the virtues of the approach and its usefulness, as follows:

1. Gold, palladium, and platinum are three of the most used metals to make contacts to nanoscale devices: as it turns out, the PPs in Ref. [8] do not reproduce lower features of the electronic dispersion properly. Sn LDA appeared as an insulator, when it clearly is a metal. The problem is remediated here.

2. Some PPs are not available on Ref. [8], and a case example is W. Here we create the PP and basis set for W. We validate the pseudo and basis with a transferability test for the relevant transition metal dichalcogenide WSe$_2$.
3. The PP for Bismuth available on Ref. [8] does not produce the electron–hole pockets for Bi. We remediated this problem here.
4. We present a new phase for stanene. These results become possible once valid and trusted PPs are available.
5. This Article highlights the use of spin–orbit-interaction within the *SIESTA* code as well.

Extensive transferability tests guarantee the usefulness of these pseudopotentials in other chemical environments. The algorithm can be applied to arbitrary elements and compounds, thus providing a viable framework and quantitative guidelines for the optimization of pseudopotentials and basis sets in SIESTA-based calculations. The extensive list of inputs aids the reader for immediate studies of a large number of novel materials of undoubted present-day relevance.

Acknowledgments

References

[1] P. Hohenberg, W. Kohn, Phys. Rev. (1964) 136.
[2] W. Kohn, L. Sham, Phys. Rev. (1965) 140.
[3] R.M. Martin, Electronic Structure: Basic Theory and Practical Methods, first ed., Cambridge U. Press, Cambridge, UK, 2004.
[4] J. Sakurai, J. Napolitano, Modern Quantum Mechanics, second ed., Addison Wesley, San Francisco, 2011. Chapter 2nd.
[5] F. Jollet, M. Torrent, N. Holzwarth, Comput. Phys. Commun. 185 (2014) 1246.
[6] K. Garrity, J. Bennett, K. Rabe, D. Vanderbilt, Comput. Mater. Sci. 81 (2014) 446.
[7] P. Blöchl, Phys. Rev. B 50 (1994) 17953.
[8] http://departments.icmab.es/leem/siesta/Databases/index.html.
[9] N. Troullier, J. Martins, Phys. Rev. B 43 (1991) 1993.
[10] Http://www.abinit.org/downloads/psp-links/psp-links/lda_fhi and http://www.abinit.org/downloads/psp-links/psp-links/gga_fhi.
[11] J. Perdew, A. Zunger, Phys. Rev. B 23 (1981) 5048.
[12] J. Perdew, Y. Wang, Phys. Rev. B 45 (1992) 13244.
[13] J. Perdew, K. Burke, M. Ernzerhof, Phys. Rev. Lett. 77 (1996) 3865.
[14] A. Walkingshaw, N. Spaldin, E. Artacho, Phys. Rev. B 70 (2004) 165110.
[15] J. Soler, E. Artacho, J. Gale, A. García, J. Junquera, P. Ordejón, D. Sánchez-Portal, J. Phys.: Condens. Matter 14 (2002) 2745.
[16] E. Artacho, E. Anglada, O. Dieguez, J. Gale, A. García, J. Junquera, R. Martin, P. Ordejón, J. Pruneda, D. Sánchez-Portal, et al., J. Phys.: Condens. Matter 20 (2008) 064208.
[17] E. Artacho, D. Sánchez-Portal, P. Ordejón, A. García, J. Soler, Phys. Stat. Sol. B 215 (1999) 809.
[18] X. Gonze, J.-M. Beuken, R. Caracas, F. Detraux, M. Fuchs, G.-M. Rignanese, L. Sindic, M. Verstraete, G. Zerah, F. Jollet, et al., Comput. Mater. Sci. 25 (2002) 478.
[19] L. Fernandez-Seivane, M.A. Oliveira, S. Sanvito, J. Ferrer, J. Phys.: Condens. Matter 18 (2006) 7999.
[20] Http://elk.sourceforge.net/.
[21] Http://www.abinit.org/downloads/psp-links/lda_tm.
[22] P. Giannozzi, S. Baroni, N. Bonini, M. Calandra, R. Car, C. Cavazzoni, D. Ceresoli, G.L. Chiarotti, M. Cococcioni, I. Dabo, et al., J. Phys.: Condens. Matter 21 (2009) 395502.
[23] M. Segall, P. Lindan, M. Probert, C. Pickard, P. Hasnip, S. Clark, M. Payne, J. Phys.: Condens. Matter 14 (2002) 2717.
[24] G. Kresse, J. Hafner, Phys. Rev. B 47 (1993) 558.
[25] J. Mozos, P. Ordejón, M. Brandbyge, J. Taylor, K. Stokbro, Nanotechnology 13 (2002) 346.
[26] M. Brandbyge, J. Mozos, P. Ordejón, J. Taylor, K. Stokbro, Phys. Rev. B 65 (2002) 165401.
[27] A. Rocha, V. Garcia-Suarez, S. Bailey, C. Lambert, J. Ferrer, S. Sanvito, Nat. Mater. 4 (2005) 335.
[28] A. Rocha, V. Garcia-Suarez, S. Bailey, C. Lambert, J. Ferrer, S. Sanvito, Phys. Rev. B 73 (2006) 085414.
[29] S. Huzinaga, J. Andzelm, M. Klobukowski, E. Radzio-Andzelm, Y. Sakai, H. Tatewaki, Gaussian Basis Sets for Molecular Calculations, Elsevier Publ. Co., Amsterdam/New York, 1984.
[30] T. van Mourik, A. Wilson, K. Peterson, D. Woon, T. Dunning Jr., Advances in Quantum Chemistry, Quantum Systems in Chemistry and Physics, Part I, Academic Press, NY, 1999.
[31] J. Lewis, P. Jelínek, J. Ortega, A. Demkov, D. Trabada, B. Haycock, H. Wang, G. Adams, J. Tomfohr, E. Abad, et al., J. Chem. Phys. 248 (2011) 1989.
[32] C.-K. Skylaris, P. Haynes, A. Mostofi, M. Payne, J. Chem. Phys. 122 (2005) 084119.
[33] O.F. Sankey, D.J. Niklewski, Phys. Rev. B 40 (1989) 3979.
[34] J. Junquera, O. Paz, D. Sanchez-Portal, E. Artacho, Phys. Rev. B 64 (2001) 235111.
[35] E. Anglada, J.M. Soler, J. Junquera, E. Artacho, Phys. Rev. B 66 (2002) 205101.
[36] F. Corsetti, M.-V. Fernandez-Serra, J. Soler, E. Artacho, J. Phys.: Condens. Matter 25 (2013) 435504.
[37] D. Hamann, M. Schlüter, C. Chiang, Phys. Rev. Lett. 43 (1979) 1494.
[38] G. Kresse, J. Joubert, Phys. Rev. B 59 (1999) 1758.
[39] S. Barraza-Lopez, M. Avery, K. Park, Phys. Rev. B 76 (2007) 224413.
[40] S. Barraza-Lopez, K. Park, V. Garcia-Suarez, J. Ferrer, Phys. Rev. Lett. 102 (2009) 246801.
[41] K. Park, S. Barraza-Lopez, V. Garcia-Suarez, J. Ferrer, Phys. Rev. B 81 (2010) 12447.
[42] G. Kresse, J. Hafner, Phys. Rev. B 49 (1994) 14251.
[43] G. Kresse, J. Furthmüller, Phys. Rev. B 54 (1996) 11169.
[44] G. Kresse, D. Joubert, Phys. Rev. B 59 (1999) 1758.
[45] L. Kleinman, D. Bylander, Phys. Rev. Lett. 48 (1982) 1425.
[46] S. Louie, S. Froyen, M. Cohen, Phys. Rev. B 26 (1982) 1738.
[47] W. Press, B. Flannery, S. Teukolsky, W. Vetterling, Numerical Recipes, Cambridge U. Press, 1989.
[48] I. Garzon, K. Michaelian, M. Beltran, A. Posada-Amarillas, P. Ordejon, E. Artacho, D. Sanchez-Portal, J. Soler, Phys. Rev. Lett. 81 (1998) 1600.
[49] K. Michaelian, N. Rendon, I. Garzon, Phys. Rev. B 60 (1999) 2000.
[50] D. Sanchez-Portal, E. Artacho, J. Junquera, P. Ordejon, A. Garcia, J. Soler, Phys. Rev. Lett. 83 (1999) 3884.
[51] I. Garzon, C. Rovira, K. Michaelian, M. Beltran, J. Junquera, P. Ordejon, E. Artacho, D. Sanchez-Portal, J. Soler, Phys. Rev. Lett. 85 (2000) 5290.
[52] X. Lopez-Lozano, L. Perez, I. Garzon, Phys. Rev. Lett. 97 (2006) 233401.
[53] O. Jepsen, A. Glötzel, A.R. Mackintosh, Phys. Rev. B 23 (1981) 2684.
[54] O.K. Anderen, Phys. Rev. B 2 (1970) 883.
[55] N.E. Christensen, Phys. Rev. B 14 (1976) 3446.
[56] P. Haas, F. Tran, P. Blaha, Phys. Rev. B 79 (2009) 085104.
[57] P. Haas, F. Tran, P. Blaha, Phys. Rev. B 79 (2009) 209902 (E).
[58] A. Barfuss, L. Dudy, M. Scholz, H. Roth, P. Höpfner, C. Blumenstein, G. Landolt, J. Dil, N. Plumb, M. Radovic, et al., Phys. Rev. Lett. 111 (2013) 157205.
[59] Y. Ohtsubo, P.L. Fèvre, F. Bertran, A. Taleb-Ibrahimi, Phys. Rev. Lett. 111 (2013) 216401.
[60] Y. Xu, B. Yan, H.-J. Zhang, J. Wang, G. Xu, P. Tang, W. Duan, S.-C. Zhang, Phys. Rev. Lett. 111 (2013) 136804.
[61] V. García-Suárez, C. Newman, C. Lambert, J. Pruneda, J. Ferrer, J. Phys.: Condens. Matter 16 (2004) 5453.
[62] J.-P. Issi, Aust. J. Phys. 32 (1979) 585.
[63] J.-P. Issi, Adv. Phys. 25 (1976) 555.
[64] J. Rose, R. Schuchardt, Phys. Status Solidi B 117 (1983) 213.
[65] X. Gonze, J.-P. Michenaud, J.-P. Vigneron, Phys. Rev. B 41 (1990) 11827.
[66] Y. Liu, R. Allen, Phys. Rev. B 52 (1995) 1566.
[67] C. Sabater, D. Gosálbez-Martínez, J. Fernández-Rossier, J. Rodrigo, C. Untiedt, J. Palacios, Phys. Rev. Lett. 110 (2013) 176802.
[68] P. Wallace, Phys. Rev. 71 (1947) 622.
[69] J.W. McClure, IBM J. Res. Dev. 8 (1964) 255.
[70] K.S. Novoselov, A.K. Geim, S.V. Morozov, D. Jiang, M.I. Katsnelson, I.V. Grigorieva, S.V. Dubonos, A.A. Firsov, Nature 438 (2005) 197.
[71] Y.B. Zhang, Y.W. Tan, H.L. Stormer, P. Kim, Nature 438 (2005) 201.
[72] C. Berger, Z. Song, T. Li, X. Li, A.Y. Ogbazghi, R. Feng, Z. Dai, A. Marchenkov, E. Conrad, P. First, et al., J. Phys. Chem. B 108 (2004) 19912.
[73] A.H. Castro Neto, F. Guinea, N.M.R. Peres, K.S. Novoselov, A.K. Geim, Rev. Mod. Phys. 81 (2009) 109.
[74] A.K. Geim, I.V. Grigorieva, Nature 499 (2013) 419.
[75] C. Jin, F. Lin, K. Suenaga, S. Iijima, Phys. Rev. Lett. 102 (2009) 195505.
[76] Q. Wang, K. Kalantar-Zadeh, A. Kis, J. Coleman, M. Strano, Nat. Nanotech. 7 (2012) 699.
[77] H.L. Zhuang, R.G. Hennig, Appl. Phys. Lett. 103 (2013) 212102.
[78] H.L. Zhuang, A.K. Singh, R.G. Hennig, Phys. Rev. B 87 (2013) 165415.
[79] H. Liu, A. Neal, Z. Zhu, Z. Luo, X. Xu, D. Tománek, P. Ye, ACS Nano 8 (2014).
[80] L. Li, Y. Yu, G. Ye, Q. Ge, X. Ou, H. Wu, D. Feng, X. Chen, Y. Zhang, Nat. Nanotech. 9 (2014).
[81] A. Pacheco-Sanjuan, Z. Wang, H. Pour-Imani, M. Vanević, S. Barraza-Lopez, Phys. Rev. B 89 (2014) 121403 (R).

[82] A. Pacheco Sanjuan, M. Mehboudi, E. Harriss, H. Terrones, S. Barraza-Lopez, ACS Nano 8 (2014) 1136.

[83] A. Castellanos-Gomez, R. Roldán, E. Capelluti, M. Buschema, F. Guinea, H.S.J. van der Zant, G.A. Steele, Nano Lett. 13 (2013) 5361.

[84] Y. Hui, X. Liu, W. Jie, N. Chan, J. Hao, Y. Hsu, L. Li, W. Guo, S. Lau, ACS Nano 7 (2013) 7126.

[85] K. He, C. Poole, K. Mak, J. Shan, Nano Lett. 13 (2013) 2931.

[86] S. Bertolazzi, J. Brivio, A. Kis, ACS Nano 5 (2011) 9703.

[87] M. Katsnelson, Graphene: Carbon in Two Dimensions, first ed., Cambridge U. Press, 2012.

[88] L.H. Brixner, J. Inorg. Nucl. Chem. 24 (1962) 257.

[89] R. Fivaz, E. Mooser, Phys. Rev. 163 (1967) 743.

[90] J.A. Wilson, A.D. Yoffee, Adv. Phys. 18 (1969) 193.

[91] T. Wieting, J. Phys. Chem. Solids 31 (1970) 2148.

[92] S. El-Mahalawy, B. Evans, Phys. Status Solidi (b) 86 (1978) 151.

[93] S. Cincotti, J. Burda, R. Hentschke, J. Rabe, J. Phys. Rev. E 51 (1995) 2090.

[94] L.F. Mattheiss, Phys. Rev. B 8 (1973) 3719.

[95] M. Hershfinke, L. Gheber, V. Volterra, J. Hutchison, L. Margulis, R. Tenne, J. Am. Chem. Soc. 116 (1994) 1914.

[96] Y. Zhu, W. Hsu, H. Terrones, N. Grobert, B. Chang, M. Terrones, B. Wei, H. Kroto, D. Walton, C. Boothroy, et al., J. Mater. Chem. 10 (2000) 2570.

[97] A. Rothschild, J. Sloan, R. Tenne, J. Am. Chem. Soc. 122 (2000) 5169.

[98] H. Li, G. Lu, Y. Wang, Z. Yin, C. Cong, Q. He, L. Wang, F. Ding, T. Yu, H. Zhang, Small 9 (2013) 1974.

[99] S. Cahangirov, M. Topsakal, E. Aktürk, H. Sahin, S. Ciraci, Phys. Rev. Lett. 102 (2009) 236804.

[100] O. Madelung, U. Rössler, M. Schulz (Eds.), Bismuth Selenide (Bi_2Se_3) Crystal Structure, Chemical Bond, Lattice Parameter (Including Data of Related Compounds), vol. 41C of The Landolt-Börnstein Database, SpringerMaterials, 2013, doi:http://dx.doi.org/10.1007/10681727_955 (Chapter).

[101] S. García-Gil, A. García, N. Lorente, P. Ordejón, J. Phys.: Condens. Matter 21 (2009) 395502.

[102] S. Nakajima, J. Phys. Chem. Solids 24 (1963) 479.

[103] H. Zhang, C.-X. Liu, X.-L. Qi, X. Dai, Z. Fang, S.-C. Zhang, Nat. Phys. 5 (2009) 438.

[104] K. Park, J. Heremans, V. Scarola, D. Minic, Phys. Rev. Lett. 105 (2010) 186801.

[105] M. Marder, Condensed Matter Physics, first ed., Wiley-Interscience, 2000.

[106] E. Zarechnaya, N. Skorodumova, S. Simak, B. Johansson, E. Isaev, Comput. Mater. Sci. 43 (2008).

[107] F. Aguilera-Granja, A. Vega, J. Rogan, W. Orellana, G. Garcia, Eur. Phys. J. D 44 (2007).

[108] A. Rüegg, S. Coh, J. Moore, Phys. Rev. B 88 (2013) 155127.

[109] P. Rivero, J.-A. Yan, V. Garcia-Suarez, J. Ferrer, S. Barraza-Lopez, Phys. Rev. B (2014) (in press).